



Stochastic Gravitational-Wave Background from the Mergers of Supermassive Black Hole Binaries

THESIS

submitted in partial fulfillment of the
requirements for the degree of

MASTER OF SCIENCE

in

ASTRONOMY AND COSMOLOGY

Author : Danial Rangavar Langeroodi

Student ID : 2238241

Supervisor : Dr. Elena M. Rossi

2nd Reader : Prof. Paul van der Werf

Leiden, The Netherlands, June 30, 2020

Stochastic Gravitational-Wave Background from the Mergers of Supermassive Black Hole Binaries

Danial Rangavar Langeroodi

Leiden Observatory, Leiden University
P.O. Box 9500, 2300 RA Leiden, The Netherlands

June 30, 2020

Abstract

LISA will enable us to resolve the stochastic gravitational-wave (GW) background, emitted by the mergers of supermassive black hole binaries (SMBHB). We showed that, by relying on the stochastic GW background in the frequency range of LISA, it is possible to 1) distinguish between different semi-analytic galaxy formation models and their SMBHB population realizations, and 2) accurately recover the cosmic distribution of SMBHBs in the intermediate mass ($M \sim 10^5 - 10^8 M_\odot$) and redshift ranges ($z \sim 5 - 11$). For each SMBHB population synthesis models considered in this work, we estimated the instrument noise limit, below which we can solely rely on the stochastic GW background to distinguish between the models, and showed that below this observational limit, the recovered population by the second method is in consistence with the distinguished model by the first method. We showed that it is possible to improve the derived constraints on the SMBHB population, by including the stochastic GW background in Decigo frequency range. Moreover, we showed that the precision of the whole analysis could be improved significantly by including the data from individually resolved binaries.

Contents

1	Introduction	1
2	Theoretical Background	5
2.1	Quadrupole Radiation: Mathematical Derivation	5
2.1.1	Weak-Field Approximation	6
2.1.2	Plane-Waves	8
2.1.3	Energy of the Plane-Waves	9
2.1.4	Quadrupole Approximation	12
2.2	Quadrupole Radiation: Physical Derivation	15
2.2.1	Transverse-Traceless Gauge	16
2.2.2	Energy	18
2.2.3	Low-Velocity Expansion	22
2.2.4	First Order (Quadrupole Radiation)	24
2.3	Mass in Circular Orbit	28
2.3.1	Chirp Amplitude	29
2.4	Stochastic Gravitational-Wave Background	32
2.4.1	Mathematical Derivation	32
2.4.2	Application to the Mergers of Binary Black Holes	34
3	Semi-Analytic Models	41
3.1	Galaxy/SMBH Coevolution Models	41
3.2	Merger Event Rates	45
4	Methods	49
4.1	Calculating the Stochastic GW Background	50
4.2	Hierarchical Bayesian Approach	52
4.2.1	Bayesian Statistics	52
4.2.2	The Odds	53

4.2.3	Hierarchical Bayesian Statistics	54
4.3	Hierarchical Bayesian Statistics in this Work	56
4.3.1	Hierarchical Framework	56
4.3.2	Posterior Distribution	58
4.4	Individually Resolved Binaries	60
4.4.1	Signal to Noise Ratio	60
4.4.2	Deriving the Priors	60
4.5	Recovering the SMBHB Population	63
4.5.1	MCMC Sampling	63
5	Results	67
5.1	Stochastic GW Background	67
5.2	Direct Model Comparison	70
5.2.1	Observed Stochastic Background	70
5.2.2	Posterior Distribution	71
5.2.3	Observational Limits	73
5.3	Individually Resolved Mergers	76
5.3.1	Simulating the Observations	76
5.3.2	Deriving the Priors from Observations	77
5.3.3	Joint Constraints	79
5.4	Recovering the Distribution of SMBHBs	81
6	Discussion	87
6.1	Hierarchical Approach	87
6.2	Recovering the Distribution	89
6.3	Individually Resolved Binaries	90
7	Conclusion	93
8	Future Prospects	95

Introduction

The emission of Gravitational-Waves (GW) from accelerating mass, is one of the predictions of the General Theory of Relativity (Einstein, 1918). In particular, we expect a substantial GW emission from the rotation of massive binary systems, such as neutron star binaries and black hole binaries (Weinberg, 1972; Gair et al., 2013; Yunes & Siemens, 2013; Berti et al., 2015). This GW emission carries energy away from the binary, causing it to harden (decrease in separation) due to the energy loss. Measuring this decay, in pulsar-timing arrays, provides indirect evidence for the emission of GWs. Since the orbital period is proportional to the separation of the binary, hardening causes a decrease in the orbital period. When one of the components of the binary is a pulsar, we can measure the orbital period with high accuracy, allowing for the detection of this decay, and acting as indirect evidence for the GW emission (Hulse & Taylor, 1975; Damour & Taylor, 1992; Kramer et al., 2006).

Regarding the direct detection of GWs, more recently, the ground-based Laser Interferometer Gravitational-Wave Observatory (Advanced LIGO) observed a transient gravitational-wave signal, with a wave-form matching the predictions of General Relativity for the inspiral of a black hole binary merger, with greater than 5.1σ significance (Abbott et al., 2016a). Since then, the advanced LIGO/VIRGO teams continued their missions by detecting the GW emission from various neutron star and black hole binaries (e.g. Abbott et al., 2016a,b, 2017). Also, within the next few years, two new ground-based detectors will join LIGO and VIRGO; the Japanese interferometer (KARGA^{*}), and a LIGO-type detector in India[†].

With the improved sensitivity of pulsar-timing arrays in $f \sim 10^{-9} -$

^{*}"KARGA", <http://gwcenter.icrr.u-tokyo.ac.jp/en/>.

[†]"IndIGO", <http://www.gw-indigo.org>.

10^{-6}Hz , they can target the coalescence of massive black holes (MBH) with masses $\sim 10^8 - 10^9 M_\odot$ (Foster & Backer, 1990). However, observational limits for resolving pulsars at high redshifts, restricts pulsar-timing arrays to the local universe, not exceeding $z = 1.5$. Similarly, due to their frequency range ($10 - 10^3\text{Hz}$), the current generation of the ground-based GW observatories can not detect the GW emission from massive black hole binaries (MBHB), nor probe the universe further than $z = 2$ (Belczynski et al., 2014a,b, 2016).

The current belief is that almost every galaxy hosts a MBH, ranging in mass from $10^4 M_\odot$ to $10^{10} M_\odot$ (Kormendy & Richstone, 1995). Galaxy mergers, followed by dynamical friction against the stellar background (Dotti & Ruszkowski, 2010; Dosopoulou & Antonini, 2017) or planet-like migration (Haiman et al., 2009; Colpi, 2014; Lodato et al., 2009), amongst many other speculated mechanisms (refer to the last parsec problem (Begelman et al., 1980)), brings these MBHs close to each other to form massive black hole binary (MBHB), which then, inspirals due to the energy loss in GWs, and finally merges. The detection of GW emission from the coalescence of MBHBs can provide us with an unprecedented probe for studying the coevolution of the galaxies and their central MBHs, structure formation models, reconstructing the cosmic history and origin of MBHs, or even, higher-order approximations of general relativity for GW emission (Plowman et al., 2010; Sesana et al., 2011; Barausse et al., 2015).

MBHBs emit GWs in $f \sim 10^{-8} - 1\text{Hz}$, which is mostly out of reach for both ground-based GW instruments, and pulsar-timing arrays. Conveniently, the new generation of ground-based (Einstein Telescope [‡]) and space GW missions (LISA [§], and Decigo: Kawamura et al. (2011)) target the frequency range of MBHBs. Semi-analytic galaxy formation simulations predict that most of the MBHB mergers will not emit a strong-enough GW signal, detectable by the future surveys (Klein et al., 2016; Dayal et al., 2019). Semi-analytic models have a proper handle on the total number of detectable MBHBs in future surveys. Comparing the total number of such events, detected in a future survey, with the predicted number from simulations, will enable us to distinguish between different prescriptions for galaxy/MBH coevolution; this is one of the highly anticipated scientific outcomes for the future GW surveys (Tanaka & Haiman, 2009; Volonteri, 2010; Barausse, 2012; Klein et al., 2016).

Although most of the MBHBs emit GWs below the sensitivity of future surveys, superposition of a large number of MBHBs creates a stochastic

[‡]<http://www.et-gw.eu>

[§]<https://lisa.nasa.gov>

gravitational-wave background (Phinney, 2001; Christensen, 2018), which, many semi-analytic models predict to be detectable by future surveys, especially LISA and Decigo (i.g. Klein et al., 2016; Dayal et al., 2019). Despite several studies addressing the total number of individually detected MBHBs as a key observation for constraining the galaxy/MBH coevolution models (Tanaka & Haiman, 2009; Volonteri, 2010; Barausse, 2012; Klein et al., 2016), the literature lacks a careful treatment of the stochastic GW background as a similar probe. In this work, we will investigate our ability in using the stochastic GW background as an observation to constrain the prescriptions in galaxy/MBH coevolution models, and study the construction history and origins of MBHBs.

First, we will use the stochastic GW background to compare the MBHB population synthesis models directly against each other. Then, we will introduce a Markov chain Monte Carlo (MCMC) approach to recover the population of MBHBs from the stochastic GW background and assess its consistency with the direct comparison approach. And finally, we will introduce a complementary method to use the measured mass and redshift of the individually detected binaries to improve our constraints on MBHB population synthesis models (we emphasize that this approach is different than what is available in the literature, which, in general, relies only on the total number of MBHBs to distinguish between different models).

The second chapter gives a brief introduction to the theory of General Relativity and its predictions for gravitational wave radiation. The third chapter is an introduction to the characteristics of the semi-analytic galaxy formation models and the MBHB realizations based on them. In the fourth chapter, we present our method to distinguish between the different galaxy formation and MBHB synthesis models both by direct comparison against the stochastic GW background, and recovering the population of MBHBs; also we will introduce our method for deriving the constraints from the individually detected binaries. In the fifth chapter, we show the results of applying our methods to the semi-analytic simulations introduced in the third chapter. Chapter six provides a discussion on the results, and chapter seven and eight present the conclusion and future prospects of this work.

Chapter 2

Theoretical Background

We decided to split the background material into two chapters. This chapter provides a brief introduction to the predictions of General Relativity for the Quadrupole Radiation of GWs, and the next chapter is devoted to introduce and discuss the semi-analytic galaxy formation models used throughout this work. In the first two sections, we will derive the general formulas concerning a source of GW with low internal velocities. Section 3, is the application of this approximation to the case of mass in a circular orbit, as a close approximation to the GW emission by massive binaries (Neutron Star and Black Hole binaries). Finally, the fourth section derives the integrated stochastic GW background resulting from the superposition of a large number of sources.

2.1 Quadrupole Radiation: Mathematical Derivation

Throughout this section, we will mainly rely on Weinberg (1972). He offers the following mathematical derivation of the concept, which is nothing short of a work-of-art. The level of clarity, completeness, and compactness is unmatched by any other source (e.g. Schutz or Poisson), and he leaves no stones unturned. The purpose of this section is to provide the necessary mathematical background and a smooth derivation of the energy emission in the Quadrupole approximation for the GW radiation. We will keep this section brief and to-the-point, to establish the necessary theoretical background, especially the Theory of General Relativity and its weak-field approximation. Our derivation of the energy carried by the GWs in this section, might seem a bit dry and lacking astrophysical motivation; we

will address this in the next section, where we provide an Astrophysically-motivated derivation of the Quadrupole approximation.

2.1.1 Weak-Field Approximation

We start by adding perturbations to the flat space-time. Starting with the Minkowski metric $\eta_{\mu\nu}$, by adding a small perturbation $h_{\mu\nu}$ (with $h_{\mu\nu} \ll 1$), the metric will turn to

$$g_{\mu\nu} = \eta_{\mu\nu} + h_{\mu\nu}, \quad (2.1)$$

with the inverse metric given by

$$g^{\mu\nu} = \eta^{\mu\nu} - h^{\mu\nu}. \quad (2.2)$$

Because

$$g^{\mu\nu} g_{\nu\rho} = \eta^{\mu\nu} \eta_{\nu\rho} + \eta^{\mu\nu} h_{\nu\rho} - h^{\mu\nu} \eta_{\nu\rho} = \delta^\mu_\rho + h^\mu_\rho - h^\mu_\rho = \delta^\mu_\rho, \quad (2.3)$$

makes 2.2 the inverse of the metric, by definition. We are interested in deriving the Einstein's field equation for this perturbed metric (2.1). Recalling the field equations here

$$R_{\mu\nu} = 8\pi G \left(T_{\mu\nu} - \frac{1}{2} T g_{\mu\nu} \right). \quad (2.4)$$

From 2.1, and 2.2, we can calculate the Christoffel symbols, which by definition are

$$\Gamma_{\mu\nu}^\rho = \frac{1}{2} g^{\rho\lambda} (\partial_\mu g_{\nu\lambda} + \partial_\nu g_{\lambda\mu} - \partial_\lambda g_{\mu\nu}). \quad (2.5)$$

Inserting 2.1, and 2.2 in the above equation and only keeping the first order terms in $h^{\mu\nu}$, we get

$$\Gamma_{\mu\nu}^\rho = \frac{1}{2} (\eta^{\rho\lambda} - h^{\rho\lambda}) \left[\partial_\mu (\eta_{\nu\lambda} + h_{\nu\lambda}) + \partial_\nu (\eta_{\lambda\mu} + h_{\lambda\mu}) - \partial_\lambda (\eta_{\mu\nu} + h_{\mu\nu}) \right] \quad (2.6)$$

$$= \frac{1}{2} \eta^{\rho\lambda} \left[\partial_\mu h_{\nu\lambda} + \partial_\nu h_{\lambda\mu} - \partial_\lambda h_{\mu\nu} \right]. \quad (2.7)$$

The Ricci Tensor in terms of the Christoffel symbols is given by

$$R_{\mu\nu} = R^\rho_{\nu\mu\rho} = g^{\rho\mu} R_{\mu\nu\rho\sigma} = g^{\rho\mu} (\eta_{\mu\lambda} \partial_\sigma \Gamma_{\nu\rho}^\lambda - \eta_{\mu\lambda} \partial_\rho \Gamma_{\nu\sigma}^\lambda). \quad (2.8)$$

Since $h_{\mu\nu}$ is small, we can use η instead of g to raise and lower the symbols in the above equation; therefore

$$R_{\mu\nu} = \eta^{\rho\mu}(\eta_{\mu\lambda}\partial_\sigma\Gamma_{\nu\rho}^\lambda - \eta_{\mu\lambda}\partial_\rho\Gamma_{\nu\sigma}^\lambda) = \sigma_\lambda^\rho\partial_\sigma\Gamma_{\nu\rho}^\lambda - \sigma_\lambda^\rho\partial_\rho\Gamma_{\nu\sigma}^\lambda = \partial_\sigma\Gamma_{\nu\lambda}^\lambda - \partial_\lambda\Gamma_{\nu\sigma}^\lambda. \quad (2.9)$$

Knowing the first order (in $h_{\mu\nu}$) Christoffel symbols from equation 2.7, first order Ricci Tensor would result by inserting 2.7 into 2.9:

$$R_{\mu\nu}^{(1)} = \frac{1}{2} \left(\square h_{\mu\nu} - \partial_\lambda\partial_\mu h_\nu^\lambda - \partial_\lambda\partial_\nu h_\mu^\lambda + \partial_\mu\partial_\nu h_\lambda^\lambda \right). \quad (2.10)$$

Inserting this into the Einstein Field Equation (equation 2.4) results

$$\square h_{\mu\nu} - \partial_\lambda\partial_\mu h_\nu^\lambda - \partial_\lambda\partial_\nu h_\mu^\lambda + \partial_\mu\partial_\nu h_\lambda^\lambda = -16\pi G S_{\mu\nu} \quad (2.11)$$

with,

$$S_{\mu\nu} = T_{\mu\nu} - \frac{1}{2}\eta_{\mu\nu}T^\lambda_\lambda. \quad (2.12)$$

Equation 2.11 gives the Einstein Field Equation for the perturbed field.

It is possible to simplify 2.11 by using the gauge invariance of the theory. By performing a coordinate transformation of the form below (with small $\partial\epsilon^\mu/\partial x^\nu$ to keep the field weak)

$$x^\mu \rightarrow x'^\mu = x^\mu + \epsilon^\mu(x), \quad (2.13)$$

the metric (2.1) transforms as

$$g'^{\mu\nu} = \frac{\partial x'^\mu}{\partial x^\lambda} \frac{\partial x'^\nu}{\partial x^\rho} g^{\lambda\rho}. \quad (2.14)$$

Taking $g'^{\mu\nu} = \eta^{\mu\nu} + h'^{\mu\nu}$ and using 2.13 and 2.2 in 2.14, to the first order we get

$$h'^{\mu\nu} = h^{\mu\nu} - \frac{\partial\epsilon^\mu}{\partial x^\lambda}\eta^{\lambda\nu} - \frac{\partial\epsilon^\nu}{\partial x^\rho}\eta^{\rho\mu}. \quad (2.15)$$

Since this is just a coordinate transformation, if $h_{\mu\nu}$ is a solution for Einstein Field Equation, so is 2.15. This describes the gauge invariance of the system. Now, by imposing this gauge invariance, we can demand the metric to satisfy

$$g^{\mu\nu}\Gamma_{\mu\nu}^\lambda = 0 \rightarrow \partial_\mu h_\nu^\mu = \frac{1}{2}\partial_\nu h_\mu^\mu, \quad (2.16)$$

in which, we used 2.7 to derive the second equation. Using our gauge freedom (2.15) is equivalent to changing our coordinate system to a coordinate which satisfies the above condition. That, we can always satisfy this by choosing the proper gauge is easy to prove - one just needs to derive an equation for ϵ^μ (in equation 2.13) satisfying this (we will not prove this here). Using 2.16 - which is called the harmonic coordinate system - in 2.4 results

$$\square h_{\mu\nu} = -16\pi S_{\mu\nu}. \quad (2.17)$$

This is our simplified field equation for the perturbation field. One solution to the above equation is the retarded potential defined as

$$h_{\mu\nu}(x, t) = 4 \int d^3x' \frac{S_{\mu\nu}(x', t - |x - x'|)}{|x - x'|}. \quad (2.18)$$

On the other hand, from the conservation of energy-momentum we have

$$\partial_\mu T^\mu_\nu = 0 \rightarrow \partial_\mu S^\mu_\nu = \frac{1}{2} \partial_\nu S^\mu_\mu. \quad (2.19)$$

Equation 2.18 is the general solution for the perturbed metric of equation 2.1. The retarded potential corresponds to the solution for the perturbed field equations close to the source of perturbation (which in the case of our interest, is the source of Gravitational Wave emission). It is easy to see from 2.17, that adding any solution of the form below to the retarded potential solution (2.18) gives a new solution for 2.17.

$$\square h_{\mu\nu} = 0 \quad (2.20)$$

Recalling that the equation 2.17 is the result of a gauge transformation (2.15), the above solution should also satisfy the harmonic coordinate system condition 2.16. We call the solutions of the type 2.20, Homogeneous Solutions.

2.1.2 Plane-Waves

We derived the general solution to the perturbed Einstein Field equations to be the retarded potential given by 2.18, with the gauge invariance of the solution defined by equation 2.20. However, as mentioned before, the retarded potential corresponds to the space-time behaviour close to the source of perturbation. In the case of gravitational waves, we are interested in the observation of a gravitational wave, far away from its source. The homogeneous solution, similar to the case of electromagnetic waves,

describes the plane wave propagation. Since we are interested detecting the gravitational waves, far from the source, we will focus the plane wave solutions throughout the rest of this work. It is also easy to see from 2.18 that a solution for the retarded potential turns to the homogeneous solution at infinity. The general solution to 2.20 is

$$h_{\mu\nu}(x) = e_{\mu\nu} \exp(ik_\lambda x^\lambda) + e_{\mu\nu}^* \exp(-ik_\lambda x^\lambda), \quad (2.21)$$

where

$$k_\lambda k^\lambda = 0. \quad (2.22)$$

We imposed the harmonic condition in the equation 2.16, to simplify the field equation and derive the homogeneous solutions. Hence, 2.21 should also satisfy the harmonic coordinate system condition; this is the case when

$$k_\mu e^\mu_\nu = \frac{1}{2} k_\nu e^\mu_\mu. \quad (2.23)$$

To show the above conditions (2.22, and 2.23), one should plug 2.21 into 2.20. Given the symmetry in $h_{\mu\nu}$, $e_{\mu\nu}$ is symmetric and is called the polarization tensor. It is interesting at this point to investigate the $e_{\mu\nu}$ tensor before proceeding with the derivation of Quadrupole radiation. Looking at "real" degrees of freedom, we can conclude that graviton - a spin-2 particle - carries the gravitational waves. To keep the derivation of Quadrupole Radiation straightforward and right-to-the-point, we postpone such investigation to section 2.2.1. The interested reader can find the details of such discussion in Weinberg (1972) (chapter 10).

2.1.3 Energy of the Plane-Waves

The main subject of this section is to calculate the energy carried by the plane wave solution of the previous section. By Fourier expansion, we can re-write the energy-momentum of the system as

$$T_{\mu\nu}(x, t) = \int d\omega \tilde{T}_{\mu\nu}(x, \omega) e^{-i\omega t}. \quad (2.24)$$

From equation 2.18, we can re-write the retarded potential solution as

$$h_{\mu\nu}(x, t) = 4 \int \frac{d^3 x'}{|x - x'|} \tilde{S}_{\mu\nu}(x', \omega) \exp \{-i\omega t + i\omega |x - x'| \}, \quad (2.25)$$

where $\tilde{S}_{\mu\nu}(x', \omega)$ is the Fourier transformation of the $S(x, t)$ in equation 2.12, given by

$$\tilde{S}_{\mu\nu}(x, \omega) = \tilde{T}_{\mu\nu}(x, \omega) - \frac{1}{2}\tilde{T}^\lambda_\lambda(x, \omega). \quad (2.26)$$

By assuming that $r = |x|$ is much larger than the source radii ($|x'|_{\max}$), we can re-write 2.25 as

$$h_{\mu\nu}(x, t) = \frac{4}{r} \exp(i\omega r - i\omega t) \int d^3x' \tilde{S}_{\mu\nu}(x', \omega) e^{-i\omega \hat{x} \cdot x'}. \quad (2.27)$$

In the limit $r \gg 1/\omega$, this becomes the solution for plane-waves:

$$h_{\mu\nu}(x, t) = e_{\mu\nu}(x, \omega) \exp(ik_\mu x^\mu), \quad (2.28)$$

with wave vector (k) and polarization tensor (e) defined as

$$\mathbf{k} = \omega \hat{x} \text{ and } k^0 = \omega \quad (2.29)$$

and

$$e_{\mu\nu}(x, \omega) = \frac{4}{r} \int d^3x' \tilde{S}_{\mu\nu}(x', \omega) e^{-ik \cdot x'}. \quad (2.30)$$

Equivalently, inserting equation 2.26 in the above definition gives

$$e_{\mu\nu}(x, \omega) = \frac{4}{r} [\tilde{T}_{\mu\nu}(\mathbf{k}, \omega) - \frac{1}{2}\eta_{\mu\nu} \tilde{T}^\lambda_\lambda(\mathbf{k}, \omega)] \quad (2.31)$$

with

$$\tilde{T}_{\mu\nu}(\mathbf{k}, \omega) = \int d^3x' \tilde{T}_{\mu\nu}(x', \omega) e^{-ik \cdot x'}. \quad (2.32)$$

Now, for the moment, instead of multiple Fourier terms in the Fourier transform of the energy-momentum tensor (2.24), we assume a single term transformation given by

$$T_{\mu\nu}(x, t) = \tilde{T}_{\mu\nu}(x, \omega) e^{-i\omega t}. \quad (2.33)$$

Applying the conservation law (2.19) on the above single Fourier term gives

$$\partial_\mu T^\mu_\nu = 0 \rightarrow \partial_i \tilde{T}^i_\nu(x, \omega) - i\omega \tilde{T}^0_\nu(x, \omega) = 0 \quad (2.34)$$

$$\rightarrow \partial_i \tilde{T}^i_\nu(x, \omega) e^{-ik \cdot x} - i\omega \tilde{T}^0_\nu(x, \omega) e^{-ik \cdot x} = 0 \quad (2.35)$$

which by integrating over dx gives

$$\rightarrow k_\mu \tilde{T}^\mu_v(\mathbf{k}, \omega) = 0. \quad (2.36)$$

Using the previously mentioned conditions, it is straightforward to calculate the power per solid angle for this single term (2.33). Since $r \gg 1/\omega$, the energy flux vector averaged over the spatial volume ($\langle t^{i0} \rangle$), is large compared to $1/\omega$. The power per solid angle is simply

$$\frac{dP}{d\Omega} = r^2 \hat{x}^i \langle t^{i0} \rangle. \quad (2.37)$$

Where $t_{\mu\nu}$ is the first significant order of perturbation in the linearized-theory, and is given by

$$t_{\mu\nu} \simeq \frac{1}{8\pi} \left[-\frac{1}{2} h_{\mu\nu} \eta^{\lambda\rho} R^{(1)}_{\lambda\rho} - \lambda\rho + \frac{1}{2} \eta_{\mu\nu} h^{\lambda\rho} R^{(1)}_{\lambda\rho} + R^{(2)}_{\mu\nu} - \frac{1}{2} \eta_{\mu\nu} \eta^{\lambda\rho} R^{(2)}_{\lambda\rho} \right]. \quad (2.38)$$

It is straightforward to show that $R^{(1)}_{\mu\nu} = 0$ (the first order Ricci tensor vanishes). Hence we need to go to higher orders in perturbation ($h_{\mu\nu}$) denoted by the second-order Ricci tensor ($R^{(2)}_{\mu\nu}$). Since the second-order Ricci tensor does not vanish here, by definition it gives the first (and most) significant contribution to $t_{\mu\nu}$ (refer to section 2.2.2 for a full derivation), hence

$$t_{\mu\nu} \simeq \frac{1}{8\pi} \left[R^{(2)}_{\mu\nu} - \frac{1}{2} \eta_{\mu\nu} \eta^{\lambda\rho} R^{(2)}_{\lambda\rho} \right]. \quad (2.39)$$

For the case of plane-waves, we can insert for $R^{(2)}_{\mu\nu}$ (which are the $R_{\mu\nu}$ terms with second order in $h_{\mu\nu}$) in terms of $h_{\mu\nu}$ given by its plane-wave solution (2.21). It results in a lengthy equation, but averaging over space and time such that $x^\mu \gg 1/\omega$ (which is how we evaluate the energy and momentum of waves in general), will kill any term in $R^{(2)}_{\mu\nu}$ which proportional to $\exp(\pm 2ik_\lambda x^\lambda)$. The only remaining terms will be the x^μ independent terms. Using the gauge symmetry again, and applying the harmonic coordinate conditions in 2.22, and 2.23

$$\langle R^{(2)}_{\mu\nu} \rangle = \frac{k_\mu k_\nu}{2} (e^{\lambda\rho*} e_{\lambda\rho} - \frac{1}{2} |e^\lambda_\lambda|^2), \quad (2.40)$$

and again using 2.22, and the above in the 2.39:

$$\langle t_{\mu\nu} \rangle = \frac{k_\mu k_\nu}{16\pi} (e^{\lambda\rho*} e_{\lambda\rho} - \frac{1}{2} |e^\lambda_\lambda|^2). \quad (2.41)$$

Now using this in the definition of the power over solid angle in equation 2.37, we obtain the power over solid angle for a single term in the Fourier transformation.

$$\frac{dP}{d\Omega} = \frac{r^2(\mathbf{k} \cdot \hat{\mathbf{x}})k^0}{16\pi} [e^{\lambda\nu\star}(x, \omega)e_{\lambda\nu}(x, \omega) - \frac{1}{2}|e^\lambda_\lambda(x, \omega)|^2]. \quad (2.42)$$

Inserting for wave-number and polarization tensor of the plane-wave solution, and keeping only the space-like components of the $T_{\mu\nu}$ (because of the conservation equation of a single term 2.36), we can write

$$\frac{dP}{d\Omega} = \frac{\omega^2}{\pi} \Lambda_{ij,lm}(\hat{\mathbf{k}}) \tilde{T}^{ij\star}(\mathbf{k}, \omega) \tilde{T}^{lm}(\mathbf{k}, \omega), \quad (2.43)$$

with Λ defined as

$$\Lambda_{ij,lm}(\hat{\mathbf{k}}) = \delta_{il}\delta_{jm} - 2\hat{k}_j\hat{k}_m\delta_{il} + \frac{1}{2}\hat{k}_i\hat{k}_j\hat{k}_l\hat{k}_m - \frac{1}{2}\delta_{ij}\delta_{lm} + \frac{1}{2}\delta_{ij}\hat{k}_l\hat{k}_m + \frac{1}{2}\delta_{lm}\hat{k}_i\hat{k}_j. \quad (2.44)$$

Taking the total energy density to be the sum of Fourier terms (same as equation 2.24), we integrate 2.43 over the whole ω space to get the total power per solid angle. Moreover, to derive the energy per solid angle, we must note that defining the energy momentum tensor as in equation 2.24, results the plane-wave solution to be an integration over ω of all the modes of the form in equation 2.28. Furthermore, looking at the gravitational wave energy-momentum tensor in equation 2.41, and recalling the equation 2.30, we see that the power over solid angle in equation 2.43 becomes a double integration over ω . Energy per solid angle would be the integration of this power over solid angle over all times:

$$\int_{-\infty}^{\infty} \exp[-i(\omega - \omega')t] dt = 2\pi\delta(\omega - \omega') \quad (2.45)$$

$$\rightarrow \frac{dE}{d\Omega} = 2\Lambda_{ij,lm}(\hat{\mathbf{k}}) \int_0^{\infty} \omega^2 \tilde{T}^{ij\star}(\mathbf{k}, \omega) \tilde{T}^{lm}(\mathbf{k}, \omega) d\omega \quad (2.46)$$

2.1.4 Quadrupole Approximation

Now we can easily derive the quadrupole radiation using the results of the previous section. To do this, we make another assumption by taking the source radius R very small compared to the wavelength (which is

proportional to $1/\omega$). This will allow us to approximate the equation 2.32 with

$$\tilde{T}_{ij}(\mathbf{k}, \omega) = \int d^3x \tilde{T}_{ij}(x, \omega). \quad (2.47)$$

Using the conservation law

$$\partial_\mu T^\mu_\nu(x, t) = 0 \rightarrow \partial_i \partial_j \tilde{T}^{ij}(x, \omega) = -\omega^2 \tilde{T}^{00}(x, \omega) \quad (2.48)$$

$$\rightarrow \tilde{T}_{ij}(\mathbf{k}, \omega) \simeq -\frac{\omega^2}{2} D_{ij}(\omega) \quad (2.49)$$

with,

$$D_{ij}(\omega) = \int d^3x x^i x^j \tilde{T}^{00}(x, \omega). \quad (2.50)$$

Inserting this in equation 2.43 gives

$$\frac{dP}{d\Omega} = \frac{\omega^6}{4\pi} \Lambda_{ij,lm}(\hat{k}) D_{ij}^*(\omega) D_{lm}(\omega), \quad (2.51)$$

and inserting in equation 2.46, for a source as the sum of Fourier modes of previous section,

$$\frac{dE}{d\Omega} = \frac{1}{2} \Lambda_{ij,lm}(\hat{k}) \int_0^\infty \omega^6 D_{ij}^*(\omega) D_{lm}(\omega) d\omega. \quad (2.52)$$

The next step is deriving the total energy emitted by integrating over the solid angle. We also need to note that the expression for D_{ij} tensors are independent of the solid angle.

$$\int d\Omega \hat{k}_i \hat{k}_j = \frac{4\pi}{3} \delta_{ij} \quad (2.53)$$

$$\int d\Omega \hat{k}_i \hat{k}_j \hat{k}_l \hat{k}_m = \frac{4\pi}{15} [\delta_{ij} \delta_{lm} + \delta_{il} \delta_{jm} + \delta_{im} \delta_{jl}] \quad (2.54)$$

$$\rightarrow \int d\Omega \Lambda_{ij,lm}(\hat{k}) = \frac{2}{15} [11\delta_{il} \delta_{jm} - 4\delta_{ij} \delta_{lm} + \delta_{im} \delta_{jl}]. \quad (2.55)$$

Inserting this in equation 2.51 results in the emitted power over a discrete frequency range as

$$P = \frac{2\omega^6}{5} [D_{ij}^*(\omega) D_{ij}(\omega) - \frac{1}{3} |D_{ii}(\omega)|^2] \quad (2.56)$$

and similarly, for energy

$$E = \frac{4\pi}{5} \int_0^\infty \omega^6 [D_{ij}^*(\omega) D_{ij}(\omega) - \frac{1}{3} |D_{ii}(\omega)|^2] d\omega. \quad (2.57)$$

The above equations (2.56 and 2.57) give the power and energy carried by plane-waves in Quadrupole approximation. This section serves as a standalone section on a purely-mathematical derivation of the Quadrupole approximation for the weak-field limit perturbation of Einstein field equations. Next section provides a more physical derivation of the Quadrupole radiation, which is especially practical for our purposes in this work and Astrophysics in general.

2.2 Quadrupole Radiation: Physical Derivation

The previous section was a review on the underlying mathematical framework and derivations necessary for concluding the main physical concepts of the Quadrupole approximation for plane-wave gravitational wave propagation in vacuum. In this section, building upon the previous derivations, we will provide the main astrophysical concepts used in a practical study of gravitational waves and their sources. In what follows, we heavily rely on Maggiore (2008).

We start with equation 2.17

$$\square h_{\mu\nu} = -16\pi S_{\mu\nu}, \quad (2.58)$$

and introduce a new field \bar{h} as

$$\bar{h}_{\mu\nu} = h_{\mu\nu} - \frac{1}{2}\eta_{\mu\nu}h \rightarrow h_{\mu\nu} = \bar{h}_{\mu\nu} - \frac{1}{2}\eta_{\mu\nu}\bar{h}, \quad (2.59)$$

where, in the second equality we inserted $\bar{h} = \eta^{\mu\nu}\bar{h}_{\mu\nu}$ in the first equation. Inserting this in the above field equation gives

$$\square(\bar{h}_{\mu\nu} - \frac{1}{2}\eta_{\mu\nu}\bar{h}) = -16\pi S_{\mu\nu} = -16\pi(T_{\mu\nu} - \frac{1}{2}\eta_{\mu\nu}T) \quad (2.60)$$

$$\rightarrow \square\bar{h}_{\mu\nu} - \frac{1}{2}\eta_{\mu\nu}\eta^{\lambda\rho}\square\bar{h}_{\rho\lambda} = -16\pi(T_{\mu\nu} - \frac{1}{2}\eta_{\mu\nu}\eta^{\lambda\rho}T_{\rho\lambda}) \quad (2.61)$$

and hence by comparison

$$\square\bar{h}_{\mu\nu} = -16\pi T_{\mu\nu}. \quad (2.62)$$

For the future reference, this new field also satisfies the Lorentz gauge

$$\partial^\mu \bar{h}_{\mu\nu} = 0. \quad (2.63)$$

Same as the case in previous section, and also for Electromagnetic fields, the solution to this field equation is the retarded potential,

$$\bar{h}_{\mu\nu}(x) = \frac{4G}{c^4} \int d^3x' \frac{1}{|x - x'|} T_{\mu\nu}(t - \frac{|x - x'|}{c}, x'). \quad (2.64)$$

Here, the harmonic solutions show themselves again. Adding any solution of the type

$$\square\bar{h}_{\mu\nu} = 0 \quad (2.65)$$

to the general solution of equation 2.64, will satisfy the field equation described by equation 2.62, and hence results in a new solution. Solutions satisfying the harmonic equation, describe the gravitational wave propagation far from the source, where $T_{\mu\nu} = 0$. It will turn out, as already discussed in sections 2.1.2 and 2.1.3, that equation 2.65 is describing plane waves propagating at the speed of light.

2.2.1 Transverse-Traceless Gauge

In section 2.1.2, we postponed the discussion on the degrees of freedom of the field $\bar{h}_{\mu\nu}$; this will be the main subject of this section. First, one needs to notice that, in the beginning, there might be no guarantee that our choice of perturbation field $h_{\mu\nu}$ in equation 2.1, is symmetric. However, we can impose symmetry using our harmonic coordinate system. Equation 2.16 allows us to assume a symmetric perturbation field from now on. A symmetric 4-by-4 tensor has 10 degrees of freedom in general. As discussed in section 2.1.1, due to the Lorentz gauge invariance of the theory (2.13), we can fix the gauge by an implementation of the harmonic coordinate system (equation 2.16). This equation imposes four conditions on $\bar{h}_{\mu\nu}$ tensor, hence reducing the degrees of freedom from 10 to 6. Nevertheless, we have not completely used the gauge invariance under coordinate transformations yet. Looking at equation 2.15, we can impose eight independent conditions on $\bar{h}_{\mu\nu}$, and so far we used four of them to simplify the field equations and obtain the retarded and homogeneous solutions. To fix the gauge completely, we can impose four new conditions on $h_{\mu\nu}$, and we have the freedom to choose them in a way to:

1. vanish the trace: $h^\lambda{}_\lambda = 0$ (1 condition) - which also results $h_{\mu\nu} = \bar{h}_{\mu\nu}$
2. set $h^{i0} = 0$ (3 conditions)

These conditions will completely fix the gauge; this is called the transverse traceless gauge.

Now we will proceed by imposing these conditions and in other words, fixing the gauge freedom. Applying the first condition to the harmonic coordinate conditions (equation 2.16), results

$$\partial_\mu h^\mu{}_\nu = 0 \rightarrow \partial^\mu h_{\mu\nu} = 0. \quad (2.66)$$

Now, fixing this gauge, there still exists two degrees of freedom in $h_{\mu\nu}$. From now on, we will call the field $h_{\mu\nu}$ in transverse-traceless gauge $h_{\mu\nu}^{TT}$. Recalling from section 2.1.2, these solutions (homogeneous solutions) are those of a plane-wave with a polarization tensor $e_{\mu\nu}$. If this plane-wave

propagates in the z direction, we can re-write the above equation as

$$x^4 h_{\mu\nu} = 0. \quad (2.67)$$

Applying three gauge conditions of the 2nd condition above, allows us to write the plane-wave solutions as

$$h_{\mu\nu}^{TT} = \begin{bmatrix} 0 & 0 & 0 & 0 \\ 0 & h_+ & h_\times & 0 \\ 0 & h_\times & -h_+ & 0 \\ 0 & 0 & 0 & 0 \end{bmatrix} \cos[\omega(t - z/c)]. \quad (2.68)$$

To simplify this, using the definition for Λ in equation 2.44, we can write

$$h_{ij}^{TT} = \Lambda_{ij,kl} h_{kl}. \quad (2.69)$$

It is easy to check that this actually satisfies the aforementioned choice of gauge with the desired two degrees of freedom in the cross and plus terms of the field. The Lambda tensor is simply projecting the symmetric $h_{\mu\nu}$ to the transverse traceless gauge.

We will focus on the case of large distance from the source ($|x - x'| = r$). Using the equations 2.69, and 2.64, and also the fact that by fixing the gauge $h_{\mu\nu} = \bar{h}_{\mu\nu}$, the general solution takes the form

$$h_{ij}^{TT}(x) = \frac{4G}{rc^4} \Lambda_{ij,kl} \int d^3x' T_{kl}(t - \frac{|x - x'|}{c}, x'), \quad (2.70)$$

an replacing T_{kl} with its Fourier transform, given by

$$T_{kl}(x) = \int \frac{dk}{(2\pi)^4} \tilde{T}_{kl}(k) e^{-ik_\lambda x^\lambda}, \quad (2.71)$$

in which $k^\lambda = (w/c, \mathbf{k})$, we can rewrite the solutions as

$$h_{ij}^{TT}(x) = \frac{4G}{rc^4} \Lambda_{ij,kl} \int d^3x' \int \frac{d\mathbf{k}}{(2\pi)^3} \frac{d\omega}{2\pi c} \tilde{T}_{kl}(\omega, \mathbf{k}) e^{-i\omega t + i\omega|x-x'|/c + i\mathbf{k}\cdot\mathbf{x}'} \quad (2.72)$$

$$= \frac{4G}{rc^4} \Lambda_{ij,kl} \int d^3x' \int \frac{d\mathbf{k}}{(2\pi)^3} \frac{d\omega}{2\pi c} \tilde{T}_{kl}(\omega, \mathbf{k}) e^{-i\omega t + i(\omega r/c) + i(\hat{n}\cdot\mathbf{x}')/c + i\mathbf{k}\cdot\mathbf{x}'}. \quad (2.73)$$

In the second equation, we inserted the first order approximation for $|x - x'|$ (with $\hat{n} = \hat{x}$ the propagation direction)

$$|x - x'| = r - x' \cdot \hat{n}. \quad (2.74)$$

Now, integrating 2.73 over d^3x' , and then $d\mathbf{k}$

$$h_{ij}^{TT}(x) = \frac{4G}{rc^4} \Lambda_{ij,kl} \int d\mathbf{k} \frac{d\omega}{2\pi c} \tilde{T}_{kl}(\omega, \mathbf{k}) e^{-i\omega t + i(\omega r/c)} \delta(\mathbf{k} - \omega \hat{n}/c), \quad (2.75)$$

and therefore

$$h_{ij}^{TT}(x) = \frac{4G}{rc^5} \Lambda_{ij,kl} \int_{-\infty}^{\infty} \frac{d\omega}{2\pi} \tilde{T}_{kl}(\omega, \omega \hat{n}/c) e^{-i\omega(t-r/c)}. \quad (2.76)$$

This is the solution in Transverse-Traceless gauge.

2.2.2 Energy

Setting aside the gauge symmetry of our theory for the moment, we want to approach the problem from a mathematical point of view without fixing any gauge. The exact form of the Einstein Field equation is,

$$R_{\mu\nu} - \frac{1}{2} g_{\mu\nu} R = -8\pi G T_{\mu\nu}. \quad (2.77)$$

Perturbing the metric with the perturbation field $h_{\mu\nu}$, and using the same notation as the previous section by denoting the first order (in perturbation field - $h_{\mu\nu}$) terms in $R_{\mu\nu}$ with $R_{\mu\nu}^{(1)}$, $R_{\mu\nu}^{(1)}$ will not satisfy the exact form of Einstein equation. Instead, we have

$$R_{\mu\nu}^{(1)} - \frac{1}{2} \eta_{\mu\nu} R^{(1)} = -8\pi G (T_{\mu\nu} + t_{\mu\nu}). \quad (2.78)$$

The $t_{\mu\nu}$ tensor holds the higher-order terms of energy momentum tensor (the price you pay for describing the metric with $R^{(1)}$ instead of R), and is the energy carried by gravitational waves (recalling the similar term defined in the previous section). Since we are only interested in the first-order terms in $h_{\mu\nu}$, we used the flat metric ($\eta_{\mu\nu}$) in the second term, instead of the perturbed metric $g_{\mu\nu}$. Subtracting these two equations (2.77, and 2.78) from each other

$$-8\pi G t_{\mu\nu} = R_{\mu\nu} - \frac{1}{2} g_{\mu\nu} R - R_{\mu\nu}^{(1)} + \frac{1}{2} \eta_{\mu\nu} \eta^{\rho\lambda} R_{\rho\lambda}^{(1)}. \quad (2.79)$$

As shown before, by a proper choice of gauge, we can set $R_{\mu\nu}^{(1)} = 0$. Hence, this equation is of no use for our current purpose. In order to produce a more useful relation for $t_{\mu\nu}$, we expand R beyond the first order, and to the second order terms in $h_{\mu\nu}$, denoting it by $R_{\mu\nu}^{(2)}$. Hence, from now on, we

are not allowed to use $\eta_{\mu\nu}$ instead of the actual metric to raise and lower indices on the first order ricci tensor. By inserting $R_{\mu\nu} = R_{\mu\nu}^{(1)} + R_{\mu\nu}^{(2)}$ into the above equation we get

$$-8\pi G t_{\mu\nu} = R_{\mu\nu}^{(1)} + R_{\mu\nu}^{(2)} - \frac{1}{2}g_{\mu\nu}R^{(1)} - \frac{1}{2}g_{\mu\nu}R^{(2)} - R_{\mu\nu}^{(1)} + \frac{1}{2}\eta_{\mu\nu}\eta^{\rho\lambda}R_{\rho\lambda}^{(1)} \quad (2.80)$$

$$= R_{\mu\nu}^{(2)} - \frac{1}{2}(\eta_{\mu\nu} + h_{\mu\nu})R^{(1)} - \frac{1}{2}(\eta_{\mu\nu} + h_{\mu\nu})R^{(2)} + \frac{1}{2}\eta_{\mu\nu}\eta^{\rho\lambda}R_{\rho\lambda}^{(1)} \quad (2.81)$$

$$= R_{\mu\nu}^{(2)} - \frac{1}{2}(\eta_{\mu\nu} + h_{\mu\nu})g^{\rho\lambda}R_{\rho\lambda}^{(1)} - \frac{1}{2}(\eta_{\mu\nu} + h_{\mu\nu})g^{\rho\lambda}R_{\rho\lambda}^{(2)} + \frac{1}{2}\eta_{\mu\nu}\eta^{\rho\lambda}R_{\rho\lambda}^{(1)} \quad (2.82)$$

$$= R_{\mu\nu}^{(2)} - \frac{1}{2}(\eta_{\mu\nu} + h_{\mu\nu})(\eta^{\rho\lambda} - h^{\rho\lambda})R_{\rho\lambda}^{(1)} - \frac{1}{2}(\eta_{\mu\nu} + h_{\mu\nu})(\eta^{\rho\lambda} - h^{\rho\lambda})R_{\rho\lambda}^{(2)} \quad (2.83)$$

$$+ \frac{1}{2}\eta_{\mu\nu}\eta^{\rho\lambda}R_{\rho\lambda}^{(1)}. \quad (2.84)$$

Ignoring the terms of order 3 and higher (in $h_{\mu\nu}$)

$$-8\pi G t_{\mu\nu} = R_{\mu\nu}^{(2)} - \frac{1}{2}h_{\mu\nu}\eta^{\rho\lambda}R_{\rho\lambda}^{(1)} + \frac{1}{2}\eta_{\mu\nu}h^{\rho\lambda}R_{\rho\lambda}^{(1)} - \frac{1}{2}\eta_{\mu\nu}\eta^{\rho\lambda}R_{\rho\lambda}^{(2)}, \quad (2.85)$$

in which, we can re-write $R_{\mu\nu}^{(1)}$ as

$$R_{\mu k}^{(1)} = \frac{1}{2} \left[\partial_\mu \partial_k h_\lambda^\lambda - \partial_\lambda \partial_k h_\mu^\lambda - \partial_\lambda \partial_\mu h_k^\lambda + \partial_\lambda \partial^\lambda h_{\mu k} \right]. \quad (2.86)$$

Imposing the choice of gauge from section 2.1.1, we need to satisfy the equation 2.20 (for the case of far from the source, as is our case of interest). Hence, the last term is equal to zero, and

$$R_{\mu k}^{(1)} = \frac{1}{2} \left[\partial_\mu \partial_k h_\lambda^\lambda - \partial_\lambda \partial_k h_\mu^\lambda - \partial_\lambda \partial_\mu h_k^\lambda \right]. \quad (2.87)$$

Now, using the conservation of energy (equation 2.16), which we repeat here

$$\partial_\lambda h_k^\lambda = \frac{1}{2} \partial_k h_\lambda^\lambda, \quad (2.88)$$

we can write the first term of the equation 2.87 as

$$\partial_\mu \partial_k h^\lambda_\lambda = \frac{1}{2} \partial_\mu \partial_k h^\lambda_\lambda + \frac{1}{2} \partial_k \partial_\mu h^\lambda_\lambda = \partial_\mu \partial_\lambda h^\lambda_k + \partial_k \partial_\lambda h^\lambda_\mu. \quad (2.89)$$

Inserting this into equation 2.87 results $R_{\mu\nu}^{(1)} = 0$ (as expected). Hence, by choosing the gauge to satisfy the harmonic coordinate condition, we can write the equation 2.85 as

$$-8\pi G t_{\mu\nu} = R_{\mu\nu}^{(2)} - \frac{1}{2} \eta_{\mu\nu} \eta^{\rho\lambda} R_{\rho\lambda}^{(2)} \quad (2.90)$$

Now, to obtain a relation for the second-order energy momentum tensor in terms of perturbation field, we need to expand $R_{\mu\nu}^{(2)}$ in terms of the field:

$$R_{\mu k}^{(2)} = -\frac{1}{2} h^{\lambda\nu} \left[\partial_k \partial_\mu h_{\lambda\nu} - \partial_k \partial_\lambda h_{\mu\nu} - \partial_\nu \partial_\mu h_{\lambda k} + \partial_\nu \partial_\lambda h_{\mu k} \right] \quad (2.91)$$

$$+ \frac{1}{4} \left[2\partial_\nu h^\nu_\sigma - \partial_\sigma h^\nu_\nu \right] \left[\partial_k h^\sigma_\mu + \partial_\mu h^\sigma_k - \partial^\sigma h_{\mu k} \right] \quad (2.92)$$

$$- \frac{1}{4} \left[\partial_\lambda h_{\sigma k} + \partial_k h_{\sigma\lambda} - \partial_\sigma h_{\lambda k} \right] \left[\partial^\lambda h^\sigma_\mu + \partial_\mu h^{\sigma\lambda} - \partial^\sigma h^\lambda_\mu \right]. \quad (2.93)$$

Inserting this into the equation 2.90 results a long equation for $t_{\mu\nu}$. But, we can drastically simplify the equations by averaging over the space-time

$$\langle R_{\mu\nu}^{(2)} \rangle = -\frac{1}{4} \langle \partial_\mu h_{\alpha\beta} \partial_\nu h^{\alpha\beta} \rangle. \quad (2.94)$$

Hence, redefining $t_{\mu\nu}$ as $t_{\mu\nu} \equiv \langle t_{\mu\nu} \rangle$, from equation 2.90 we can write

$$t_{\mu\nu} = \frac{c^4}{32\pi G} \langle \partial h_{\alpha\beta} \partial_\nu h^{\alpha\beta} \rangle. \quad (2.95)$$

Now, to measure the energy carried by GWs, we use the energy conservation to get

$$\int d^3x \partial_0 t^{00} = - \int d^3x \partial_i t^{i0}. \quad (2.96)$$

The left-hand side term is the energy contained in volume V

$$E_V = \int d^3x t^{00} \rightarrow \frac{dE_V}{cdt} = - \int d^3x \partial_0 t^{00}. \quad (2.97)$$

Inserting this in the energy conservation above and using Gauss's theorem, with n^i as the normal to the surface, we get

$$\frac{dE_V}{dt} = - \int dA n_i t^{0i}. \quad (2.98)$$

We can take the normal to be in the radial direction from the source, and hence

$$\frac{dE_V}{dt} = - \int dA t^{0r}. \quad (2.99)$$

Now, to calculate the term inside the integral, we recall that $t_{\mu\nu}$ is a function of the field, and by sitting in the TT gauge, we can write it as (ideally one should prove that sitting in this gauge does not change our description of the energy momentum tensor in terms of the field, which we skip here. Interested reader can find the proof in (Weinberg, 1972) and Maggiore (2008))

$$t^{0r} = \frac{c^4}{32\pi G} \langle \partial^0 h_{ij}^{TT} \frac{\partial}{\partial r} h_{ij}^{TT} \rangle. \quad (2.100)$$

The field is (as shown in sections 2.1.1 and 2.1.2) a retarded function of time (f), therefore

$$h_{ij}^{TT} = \frac{1}{r} f_{ij}(t - r/c) \rightarrow \partial_r h_{ij}^{TT} = \frac{1}{r^2} f_{ij}(t - r/c) + \frac{\partial}{r \partial r} f_{ij}(t - r/c) \quad (2.101)$$

$$\rightarrow \partial_r h_{ij}^{TT} = -\frac{\partial}{rc \partial t} f_{ij}(t - r/c) \rightarrow \partial_r h_{ij}^{TT} = -\partial_0 h_{ij}^{TT} + \text{higher orders in } 1/r. \quad (2.102)$$

Inserting this into equation 2.100 results

$$t^{0r} = t^{00}, \quad (2.103)$$

and finally, by writing the surface element as $A = r^2 d\Omega$ we can rewrite 2.99 as

$$\frac{dE_V}{dt} = - \int dA t^{0r} = \frac{c^3 r^2}{32\pi G} \int d\Omega \dot{h}_{ij}^{TT} \dot{h}_{ij}^{TT}, \quad (2.104)$$

or,

$$\frac{dE}{d\Omega} = \frac{c^3 r^2}{32\pi G} \int_{-\infty}^{\infty} dt \dot{h}_{ij}^{TT} \dot{h}_{ij}^{TT}. \quad (2.105)$$

Now, using the expression 2.76, we can write this in the more convenient form

$$\frac{dE}{d\Omega} = \frac{G}{2\pi^2 c^7} \Lambda_{ij,kl} \int_0^\infty d\omega \omega^2 \tilde{T}_{ij}(\omega, \omega \hat{n}/c) \tilde{T}_{kl}^*(\omega, \omega \hat{n}/c) \quad (2.106)$$

2.2.3 Low-Velocity Expansion

We can further simplify the equations for GW emission by assuming small internal source-velocities. This means that the typical frequencies in the source are small compared to the speed of light. If ω_s is a typical internal frequency and d its attributed distance, low-velocity limit means that

$$v \ll c \rightarrow \omega_s d \ll c. \quad (2.107)$$

Starting with equation 2.70, we can expand the Fourier transform of $T_{\mu\nu}$ in equation 2.71, using $\omega_s d \ll c$. Since the energy momentum is only non-vanishing inside the source (which is our initial assumption), we can take the integral over small $|x'|$. Hence, we can expand T_{kl} as

$$T_{kl}(t - \frac{r}{c} + \frac{x' \cdot \hat{n}}{c}, x') = \int \frac{d^4 k}{(2\pi)^4} \tilde{T}_{kl}(\omega, k) \exp(-i\omega(t - \frac{r}{c} + \frac{x' \cdot \hat{n}}{c}) + ik \cdot x') \quad (2.108)$$

$$= T_{kl}(t - \frac{r}{c}, x') + \frac{x'^i n^i}{c} \partial_0 T_{kl} + \frac{1}{2c^2} x'^i x'^j n^i n^j \partial_0^2 T_{kl} + \dots \quad (2.109)$$

inserting this in equation 2.70:

$$h_{ij}^{TT}(t, x) = \quad (2.110)$$

$$\frac{4G}{rc^4} \Lambda_{ij,kl} \left[S^{kl}(t - \frac{r}{c}) + \frac{1}{c} n_m \dot{S}^{kl,m}(t - \frac{r}{c}) + \frac{1}{2c^2} n_m n_p \ddot{S}^{kl,mp}(t - \frac{r}{c}) + \dots \right]. \quad (2.111)$$

With the momenta of the stress-tensor defined as

$$S^{ij}(t) = \int d^3 x T^{ij}(t, x) \quad (2.112)$$

$$S^{ij,k}(t) = \int d^3 x T^{ij}(t, x) x^k \quad (2.113)$$

$$S^{ij,kl}(t) = \int d^3x T^{ij}(t, x) x^k x^l. \quad (2.114)$$

We can also define the momenta of energy density T^{00}/c^2 and linear momentum T^{0i}/c as (which follows naturally from the above definition)

$$M = \frac{1}{c^2} \int d^3x T^{00}(t, x) \quad (2.115)$$

$$M^i = \frac{1}{c^2} \int d^3x T^{00}(t, x) x^i \quad (2.116)$$

$$M^{ij} = \frac{1}{c^2} \int d^3x T^{00}(t, x) x^i x^j \quad (2.117)$$

$$M^{ijk} = \frac{1}{c^2} \int d^3x T^{00}(t, x) x^i x^j x^k \quad (2.118)$$

and,

$$P^i = \frac{1}{c} \int d^3x T^{0i}(t, x) \quad (2.119)$$

$$P^{i,j} = \frac{1}{c} \int d^3x T^{0i}(t, x) x^j \quad (2.120)$$

$$P^{i,jk} = \frac{1}{c} \int d^3x T^{0i}(t, x) x^j x^k \quad (2.121)$$

Now, to calculate the integrals, we can take a big volume compared to the source, for which the energy momentum tensor vanishes at the boundary (which is again, the first assumption of plane-waves). Then, as proved in section 2.2.2

$$\partial_0 T^{00} = -\partial_i T^{0i} \rightarrow c\dot{M} = \int_V d^3x \partial_0 T^{00} = - \int_V d^3x \partial_i T^{0i}. \quad (2.122)$$

By applying Gauss's theorem, this gives

$$= - \int_{\partial V} dS^i T^{0i} = 0. \quad (2.123)$$

The last equality follows since we took the volume large enough for T to vanish at the boundary. This is the conservation of mass, which, is not exact, but approximately correct: since we are ignoring the back reaction

of the gravitational wave emission on the source itself. Applying the same line of proof to the rest of the momenta(s) results

$$\dot{M} = 0, \quad (2.124)$$

$$\dot{M}^i = P^i \quad (2.125)$$

$$\dot{M}^{ij} = P^{i,j} + P^{j,i} \quad (2.126)$$

$$\dot{M}^{ijk} = P^{i,jk} + P^{j,ki} + P^{k,ij} \quad (2.127)$$

and,

$$\dot{P}^i = 0 \text{ (conservation of total momentum)} \quad (2.128)$$

$$\dot{P}^{i,j} = S^{ij} \quad (2.129)$$

$$\dot{P}^{i,jk} = S^{ij,k} + S^{ik,j}. \quad (2.130)$$

Using these equations, it is possible to describe the momenta S^{ij} and \dot{S}^{ijk} in terms of the energy density momenta(s), and linear momentum

$$S^{ij} = \frac{1}{2} \ddot{M}^{ij} \quad (2.131)$$

$$\dot{S}^{ij,k} = \frac{1}{6} \ddot{M}^{ijk} + \frac{1}{3} (\ddot{P}^{i,jk} + \ddot{P}^{j,ik} - 2\ddot{P}^{k,ij}) \quad (2.132)$$

2.2.4 First Order (Quadrupole Radiation)

Using equation 2.111, and replacing S^{ij} by its expression in 2.131, and ignoring the higher-order terms to write down the leading term contributing to the GW emission, we get

$$[h_{ij}^{TT}(t, x)]_{\text{quad}} = \frac{2G}{rc^4} \Lambda_{ij,kl} \ddot{M}^{kl} (t - \frac{r}{c}). \quad (2.133)$$

For every tensor $M^{\mu\nu}$ we can split it to the traceless and the trace components

$$M^{kl} = (M^{kl} - \frac{1}{3} \delta^{kl} M^i_i) + \frac{1}{3} \delta^{kl} M^i_i. \quad (2.134)$$

We define the quadrupole moment as the first term:

$$Q^{ij} = M^{ij} - \frac{1}{3}\delta^{ij}M^\lambda_\lambda = \int d^3x \rho(t, x) \left(x^i x^j - \frac{1}{3}r^2 \delta^{ij} \right) \quad (2.135)$$

in which ρ is simply T^{00}/c^2 . Using this in the field expression above, and noting that the effect of Lambda ($\Lambda_{ij,kl}$) on δ^{ij} is zero, we get

$$[h_{ij}^{TT}(t, x)]_{\text{quad}} = \frac{2G}{rc^4} \ddot{Q}_{kl}^{TT} \left(t - \frac{r}{c} \right) \quad (2.136)$$

in which

$$\ddot{Q}_{kl}^{TT} \left(t - \frac{r}{c} \right) = \Lambda_{ij,kl} \ddot{Q}_{kl} \left(r - \frac{r}{c} \right). \quad (2.137)$$

Recalling from 2.68, by using our two remaining degrees of freedom, we can express the emitted plane-waves by two polarizations, plus and cross. Using the expression for Lambda tensor ($\Lambda_{ij,kl}$) in 2.44, and using the projector $P_{ij} = (0, 1, 1, 0)$ which is equivalent to assuming propagation in the z direction, we can rewrite Lambda as

$$\Lambda_{ij,kl} \ddot{M}_{kl} = \left[P_{ik} P_{jl} - \frac{1}{2} P_{ij} P_{kl} \right] \ddot{M}_{kl} \quad (2.138)$$

$$\rightarrow \Lambda_{ij,kl} \ddot{M}_{kl} = \left[\begin{array}{ccc} (\ddot{M}_{11} - \ddot{M}_{22})/2 & \ddot{M}_{12} & 0 \\ \ddot{M}_{21} & -(\ddot{M}_{11} - \ddot{M}_{22})/2 & 0 \\ 0 & 0 & 0 \end{array} \right]_{ij} \quad (2.139)$$

Hence, by comparison

$$h_+ = \frac{G}{rc^4} (\ddot{M}_{11} - \ddot{M}_{22}) \quad (2.140)$$

$$h_\times = \frac{2G}{rc^4} \ddot{M}_{12}. \quad (2.141)$$

We have calculated the momenta in above equations using the retarded time. Now we want to make a coordinate transformation from the coordinate system in which the wave propagates is in \hat{z} direction, to a more general coordinate system in which it propagates in \hat{n} direction. Assuming that u and v make an orthonormal coordinate system alongside n , we seek a coordinate transformation from $x, y, z = n'^1, n'^2, n'^3$ to $u, v, n = n^1, n^2, n^3$. We define this by the transformation tensor R^μ_ν

$$R^\mu_\nu = \left(\begin{bmatrix} 1 & 0 & 0 & 0 \\ 0 & \cos\phi & \sin\phi & 0 \\ 0 & -\sin\phi & \cos\phi & 0 \\ 0 & 0 & 0 & 1 \end{bmatrix} \begin{bmatrix} 1 & 0 & 0 & 0 \\ 0 & 1 & 0 & 0 \\ 0 & 0 & \cos\theta & \sin\theta \\ 0 & 0 & -\sin\theta & \cos\theta \end{bmatrix} \right)_{\mu\nu} \quad (2.142)$$

in which $n^\mu = R^\mu_\nu n'^\nu$ and $n^i = (n^0, \sin\theta\sin\phi, \sin\theta\cos\phi, \cos\theta)$. For $M^{\mu\nu}$ we have $M^{\mu\nu} = R^\mu_k R^\nu_l M'^{kl}$, Or equivalently $M'^{\mu\nu} = B^\mu_k B^\nu_l M^{kl}$, in which $B = (A^T)^{-1}$, given by

$$B^\mu_\nu = \begin{bmatrix} 1 & 0 & 0 & 0 \\ 0 & \cos\phi & \sin\phi\cos\theta & \sin\phi\sin\theta \\ 0 & -\sin\phi & \cos\phi\cos\theta & \cos\phi\sin\theta \\ 0 & 0 & -\sin\theta & \cos\theta \end{bmatrix}_{\mu\nu}. \quad (2.143)$$

Hence

$$h_+(t; \theta, \phi) = \frac{G}{rc^4} \left[\ddot{M}_{11}(\cos^2\phi - \sin^2\phi\cos^2\theta) + \ddot{M}_{22}(\sin^2\phi - \cos^2\phi\cos^2\theta) \right. \quad (2.144)$$

$$\left. - \ddot{M}_{33}\sin^2\theta - \ddot{M}_{12}\sin 2\phi(1 + \cos^2\phi) + \ddot{M}_{13}\sin\phi\sin 2\theta + \ddot{M}_{23}\cos\phi\sin 2\theta \right] \quad (2.145)$$

and,

$$h_\times(t; \theta, \phi) = \frac{G}{rc^4} \left[(\ddot{M}_{11} - \ddot{M}_{22})\sin 2\phi\cos\theta + 2\ddot{M}_{12}\cos 2\phi\cos\theta \right. \quad (2.146)$$

$$\left. - 2\ddot{M}_{13}\cos\phi\sin\theta + 2\ddot{M}_{23}\sin\phi\sin\theta \right] \quad (2.147)$$

To derive the first order (quadrupole) radiated energy, using equation 2.104, for the power, we can write

$$\frac{dP}{d\Omega} = \frac{c^3 r^2}{32\pi G} \langle \dot{h}_{ij}^{TT} \dot{h}_{ij}^{TT} \rangle, \quad (2.148)$$

which using 2.136, and 2.55, gives

$$\frac{dP}{d\Omega} = \frac{G}{8\pi c^5} \Lambda_{ij,kl} \langle \ddot{Q}_{ij}^{TT} \ddot{Q}_{kl}^{TT} \rangle \rightarrow P_{quad} = \frac{G}{5c^2} \langle \ddot{Q}_{ij}^{TT} \ddot{Q}_{ij}^{TT} \rangle. \quad (2.149)$$

Finally, for energy, integrating the first part of the above equation over time, and inserting the Fourier transform of Q_{ij}

$$Q_{ij}(t) = \int_{-\infty}^{\infty} \frac{d\omega}{2\pi} Q_{ij}(\omega) \exp(-i\omega t) \rightarrow \quad (2.150)$$

$$\frac{dE}{d\Omega} = \frac{G}{8\pi^2 c^5} \Lambda_{ij,kl} \int_0^\infty d\omega \omega^6 Q_{ij}(\omega) Q_{kl}^*(\omega), \quad (2.151)$$

which again, using 2.55, gives

$$E_{quad} = \frac{G}{5\pi c^5} \int_0^\infty d\omega \omega^6 Q_{ij}(\omega) Q_{kl}^*(\omega), \quad (2.152)$$

giving the energy of the gravitational wave radiation in the Quadrupole approximation.

2.3 Mass in Circular Orbit

In this section, we will specialize the Quadrupole approximation of the gravitational wave radiation to the case of a point-mass rotating in a circular orbit, which is a close approximation for most of the sources of gravitational waves, such as Binary Neutron Stars and Binary Black Holes.

We start with the energy momentum tensor of a point mass particle:

$$T^{\mu\nu}(t, x) = \frac{p^\mu p^\nu}{\gamma m} \delta^{(3)}(x - x_0(t)), \quad (2.153)$$

where $\gamma = (1 - v^2/c^2)^{-1/2}$, $p^\mu = \gamma m(dx_0^\mu/dt) = (E/c, \mathbf{p})$. Inserting this in equation 2.117, for 2 particles in a non-relativistic system we obtain

$$M^{ij} = m x_{cm}^i x_{cm}^j + \mu (x_{cm}^i x_0^j + x_{cm}^j x_0^i) + \mu x_0^i x_0^j, \quad (2.154)$$

in which μ, m are the reduced and total mass of the system, respectively. Setting the origin of the coordinate system at the centre of mass results

$$M^{ij}(t) = \mu x_0^i(t) x_0^j(t). \quad (2.155)$$

For a (non-relativistic) binary system of point masses, the relative coordinates of particles undergo a circular motion in x-y plane, with non-relativistic velocities

$$x_0(t) = R \cos(\omega_s t + \pi/2) \quad (2.156)$$

$$y_0(t) = R \sin(\omega_s t + \pi/2) \quad (2.157)$$

$$z_0(t) = 0 \quad (2.158)$$

with

$$\omega_s^2 = \frac{Gm}{R^3} \quad (2.159)$$

The above equation is only valid for constant radii (meaning that the radius of motion is not a function of time - we will discuss the general case shortly). By inserting this in the above expression for M^{ij} , we get

$$M_{11} = \mu R^2 \frac{1 - \cos 2\omega_s t}{2} \quad (2.160)$$

$$M_{22} = \mu R^2 \frac{1 + \cos 2\omega_s t}{2} \quad (2.161)$$

$$M_{12} = -\frac{1}{2}\mu R^2 \sin 2\omega_s t. \quad (2.162)$$

Using this in equations 2.144 and 2.147,

$$h_+(t; \theta, \phi) = \frac{4G\mu\omega_s^2 R^2}{rc^4} \left(\frac{1 + \cos^2 \theta}{2} \right) \cos(2\omega_s t_{ret} + 2\phi) \quad (2.163)$$

$$h_\times(t; \theta, \phi) = \frac{4G\mu\omega_s^2 R^2}{rc^4} \left(\frac{1 + \cos^2 \theta}{2} \right) \cos \theta \sin(2\omega_s t_{ret} + 2\phi). \quad (2.164)$$

Now, defining $f_{gw} = \omega_{gw}/2\pi$ with $\omega_{gw} = 2\omega_s$, and also defining the Chirp Mass as

$$M_c = \mu^{3/5} m^{2/5}, \quad (2.165)$$

we can rewrite the field expressions above as

$$h_+(t; \theta, \phi) = \frac{4}{r} \left(\frac{GM_c}{c^2} \right)^{5/3} \left(\frac{\pi f_{gw}}{c} \right)^{2/3} \frac{1 + \cos^2 \theta}{2} \cos(2\pi f_{gw} t_{ret} + 2\phi) \quad (2.166)$$

$$h_\times(t; \theta, \phi) = \frac{4}{r} \left(\frac{GM_c}{c^2} \right)^{5/3} \left(\frac{\pi f_{gw}}{c} \right)^{2/3} \cos \theta \sin(2\pi f_{gw} t_{ret} + 2\phi) \quad (2.167)$$

These are the field equations for point-like mass in circular orbit with a constant radii.

2.3.1 Chirp Amplitude

As mentioned earlier, the above equations hold only for the case of circular motion with constant radii. In this section, we want to take into account the source energy loss due to gravitational wave emission. The main effect of this energy loss is reducing the separation of binary. The total energy of the binary is the sum of kinetic and potential terms

$$E_{orbit} = E_{kin} + E_{pot} = -\frac{Gm_1 m_2}{2R} \quad (2.168)$$

A fraction of the total energy is radiated away by gravitational waves. Therefore the total energy decreases over time; equivalently, R is getting smaller. Changing R in the above equation changes the ω_s in 2.159. Here, we make one more simplification (which is justified by the fact that the energy carried by the gravitational waves is very small compared to the

total orbital energy of the binary), assuming that $\dot{\omega}_s \ll \omega_s^2$ (quasi-circular motion).

We rewrite the orbital energy in terms of Chirp Mass M_c (equation 2.165), taking $\omega_{gw} = 2\omega_s$ and using equation 2.159:

$$E_{orbit} = -\left(\frac{G^2 M_c^5 \omega_{gw}^2}{32}\right)^{1/3}. \quad (2.169)$$

In this form, orbital energy is independent of the separation. We can define the radiation power as the gravitational energy emitted over time

$$P = -\frac{dE_{orbit}}{dt}. \quad (2.170)$$

Using the equation 2.169

$$P = \frac{G^2 M_c^5}{32} \omega_{gw}^{-1/3} \dot{\omega}_{gw}. \quad (2.171)$$

On the other hand, from equation 2.148

$$\frac{dP}{d\Omega} = \frac{r^2 c^3}{16\pi G} \langle \dot{h}_+^2 + \dot{h}_\times^2 \rangle. \quad (2.172)$$

Inserting the results of constant R (when the separation is constant) for polarization fields (equations 2.163 and 2.164) into the above equation, and noting that $\langle \cos^2(2\omega t + 2\phi) \rangle = \langle \sin^2(2\omega t + 2\phi) \rangle = 1/2$, we get

$$\frac{dP}{d\Omega} = \frac{2c^5}{\pi G} \left(\frac{GM_c \omega_{gw}}{2c^3} \right)^{10/3} \left[\left(\frac{1 + \cos^2\theta}{2} \right)^2 + \cos^2\theta \right], \quad (2.173)$$

and since

$$\int \frac{d\Omega}{4\pi} \left[\left(\frac{1 + \cos^2\theta}{2} \right)^2 + \cos^2\theta \right] = \frac{4}{5}, \quad (2.174)$$

for the power we get

$$P = \frac{32c^5}{5G} \left(\frac{GM_c \omega_{gw}}{2c^3} \right)^{10/3}. \quad (2.175)$$

Now, setting equations 2.171 and 2.175 equal to each other

$$\dot{\omega}_{gw} = \frac{12}{5} 2^{1/3} \left(\frac{GM_c}{c^3} \right)^{5/3} \omega_{gw}^{11/3} \quad (2.176)$$

replacing ω with f , using $f = \omega/2\pi$

$$\dot{f}_{gw} = \frac{96}{5}\pi^{8/3}\left(\frac{GM_c}{c^3}\right)^{5/3}f_{gw}^{11/3}. \quad (2.177)$$

Integrating the above equation, and introducing the t_{coal} (coalescence time) as the time at which f_{gw} diverges (existence of such a solution is trivial because of the form of the above equation)

$$f_{gw}(t) = \frac{1}{\pi}\left(\frac{5}{256(t_{coal} - t)}\right)^{3/8}\left(\frac{GM_c}{c^3}\right)^{-5/8}, \quad (2.178)$$

or setting $\tau = t_{coal} - t$ (time to coalescence)

$$f_{gw}(\tau) = \frac{1}{\pi}\left(\frac{5}{256\tau}\right)^{3/8}\left(\frac{GM_c}{c^3}\right)^{-5/8}. \quad (2.179)$$

Using equation 2.159, for the time to coalescence τ_0 , from the above equation we get

$$\tau_0 = \frac{5}{256}\frac{c^5 r_0^4}{G^3 m^2 \mu}. \quad (2.180)$$

Now, we want to find the polarization field for this Quasi-Circular orbit. A particle that moves on a quasi-circular orbit in the x-y plane with a radius $R = R(t)$ and angular velocity $\omega_s = \omega_s(t)$ has coordinates

$$x(t) = R(t)\cos(\Phi(t)/2) \quad (2.181)$$

$$y(t) = R(t)\sin(\Phi(t)/2) \quad (2.182)$$

with

$$\Phi(t) = 2 \int_{t_0}^t dt' \omega_s(t') = \int_{t_0}^t dt' \omega_{gw}(t'). \quad (2.183)$$

We can derive the polarization fields from equations 2.163, and 2.164, by replacing $\omega_{gw}t$ with $\Phi(t)$, and also noting that, as approximated throughout this section, radial velocity \dot{R} is negligible; hence

$$h_+(t) = \frac{4}{r}\left(\frac{GM_c}{c^2}\right)^{5/3}\left(\frac{\pi f_{gw}(t_{ret})}{c}\right)^{2/3}\frac{1 + \cos^2 \iota}{2}\cos[\Phi(t_{ret})] \quad (2.184)$$

$$h_\times(t) = \frac{4}{r}\left(\frac{GM_c}{c^2}\right)^{5/3}\left(\frac{\pi f_{gw}(t_{ret})}{c}\right)^{2/3}\cos \iota \sin[\Phi(t_{ret})] \quad (2.185)$$

Since we are interested in the radiation in the direction pointing from the source toward the observer, the angle θ is equal to the angle ι between the normal to the orbit and the line of sight.

2.4 Stochastic Gravitational-Wave Background

Thus far, we discussed the gravitational wave emission of individual inspiraling binaries. In this section, we introduce the method to calculate the stochastic background emission resulted from a cosmic distribution of binary mergers. What follows is mainly based on Phinney (2001).

2.4.1 Mathematical Derivation

First, we provide the mathematical derivation for integrating the superposition of individual binaries into a stochastic background. In section 5.1, we will apply this to the case of cosmic distribution of Massive Black Hole Binaries to obtain the stochastic GW background signal emitted by such events.

The flux of gravitational wave for a distant source is given by

$$S(t) = \frac{c^3}{16\pi G} (\dot{h}_+^2 + \dot{h}_\times^2) \quad (2.186)$$

In which $+$ and \times denote the polarization of the signal as before. The Fourier transform of the polarization fields is

$$h_{+,\times}(f) = \int_{-\infty}^{\infty} h_{+,\times}(t) \exp(-i2\pi ft) dt, \quad (2.187)$$

or equivalently

$$h_{+,\times}(t) = \int_{-\infty}^{\infty} h_{+,\times}(f) \exp(i2\pi ft) dt. \quad (2.188)$$

Similarly, the Fourier Transform of the time derivative of the field is

$$\dot{h}_{+,\times}(f) = \int_{-\infty}^{\infty} \dot{h}_{+,\times}(t) \exp(-i2\pi ft) dt, \quad (2.189)$$

which, using the equation 2.188, results

$$\dot{h}_{+,\times}(f) = 2\pi i f h_{+,\times}(f). \quad (2.190)$$

On the other hand, we integrate the flux over time to derive the energy per solid angle

$$\int_{-\infty}^{\infty} S(t) dt = \frac{c^3}{16\pi G} \int_{-\infty}^{\infty} (\dot{h}_+^2(t) + \dot{h}_\times^2(t)) dt, \quad (2.191)$$

which using Parseval's equality and 2.190 gives

$$\int_{-\infty}^{\infty} S(t)dt = \frac{\pi c^3}{2G} \int_0^{\infty} f^2(|h_+^2(f)| + |h_{\times}^2(f)|)df. \quad (2.192)$$

Luminosity is equal to the average of flux over source orientations (or equivalently, over observer positions around a given source) times the whole sky surface for that source $4\pi d_L^2$. Hence

$$\langle S(t) \rangle_{\Omega_s} = \frac{L(t)}{4\pi d_L^2}. \quad (2.193)$$

Here, luminosity is measured in the source rest frame. The time, measured in source rest frame t_r , is related to the observer time t by $t = (1+z)t_r$. If we integrate the average flux over the observer time we get

$$\int_{-\infty}^{\infty} \langle S(t) \rangle_{\Omega_s} dt = \frac{1+z}{4\pi d_L^2} \int_{-\infty}^{\infty} L(t_r) dt_r = \frac{1+z}{4\pi d_L^2} E, \quad (2.194)$$

with energy (E) measured in the source rest frame. Comparing this equation and 2.192, and using $df = (1+z)^{-1}df_r$

$$\frac{1+z}{4\pi d_L^2} E = \frac{1+z}{4\pi d_L^2} \int_0^{\infty} \frac{dE}{df_r} df_r = \frac{\pi c^3}{2G(1+z)} \int_0^{\infty} f^2 \langle |h_+(f)|^2 + |h_{\times}(f)|^2 \rangle_{\Omega_s} df_r \quad (2.195)$$

$$\rightarrow \frac{dE}{df_r} = \frac{2\pi^2 c^3}{G} d_M^2 f^2 \langle |h_+(f)|^2 + |h_{\times}(f)|^2 \rangle_{\Omega_s} df_r \quad (2.196)$$

where proper distance d_M is defined as $d_L/(1+z)$.

We define \dot{N} as the event rate per comoving volume per unit of time at source rest frame, at redshift z . For the number of events per redshift, per unit of time at source rest frame we have

$$\frac{d\#}{dt_r dz} = \dot{N} \frac{dV_{com}}{dz} \rightarrow \frac{d\#}{dt dz} = \dot{N} \frac{1}{1+z} \frac{dV_{com}}{dz}, \quad (2.197)$$

where the second equation gives the number of events per unit observer time, per unit redshift. We can insert for the comoving volume from

$$\frac{dV_{com}}{dz} = 4\pi \frac{c}{H_0} d_M^2 \frac{1}{E(z)}, \quad (2.198)$$

with $E(z)$ defined as

$$E(z) = (\Omega_M(1+z)^3 + \Omega_k(1+z)^2 + \Omega_{\Lambda})^{\frac{1}{2}}. \quad (2.199)$$

Also, the number of events happening in comoving volume between times $t_r(z)$ and $t_r(z + dz)$ is

$$N(z) = \dot{N} \frac{dt_r}{dz} = \dot{N} \frac{1}{(1+z)H_0 E(z)}. \quad (2.200)$$

Hence we can rewrite 2.197 as

$$\frac{d\#}{dtdz} = N(z)c4\pi d_M^2. \quad (2.201)$$

For the energy density at $z = 0$, per logarithmic frequency

$$\epsilon_{gw} = \int \Omega_{gw}(f) \rho_c c^2 df / f = \int_0^\infty \frac{1}{c} \left[\int_{-\infty}^\infty \langle S(t) \rangle_{\Omega_s} dt \right] \frac{d\#}{dtdz} dz, \quad (2.202)$$

In which $\frac{1}{c} \int_{-\infty}^\infty \langle S(t) \rangle_{\Omega_s} dt$ is the energy per event, and $d\# / dtdz$ is the number of events per comoving volume. Now, using equations 2.194 and 2.201, the above equation is equal to

$$\int_0^\infty \frac{1+z}{4\pi d_L^2 c} \left[\int_0^\infty f_r \frac{dE_{gw}}{df_r} \frac{df}{f} \right] N(z) c 4\pi d_M^2 dz \quad (2.203)$$

$$= \int_0^\infty \int_0^\infty N(z) \frac{1}{1+z} \left(f_r \frac{dE_{gw}}{df_r} \right)_{f_r=f(1+z)} dz \frac{df}{f}, \quad (2.204)$$

which, compared to equation 2.202, results

$$\rho_c c^2 \Omega_{gw}(f) = \int_0^\infty N(z) \frac{1}{1+z} \left(f_r \frac{dE_{gw}}{df_r} \right)_{f_r=f(1+z)} dz \quad (2.205)$$

Hence, the comoving number density of events times the energy per logarithmic frequency interval for each event, gives the energy density of gravitational waves per log frequency.

2.4.2 Application to the Mergers of Binary Black Holes

Here, we will apply the results of the previous section to a population of binary black holes. For a circular binary, with masses M_1 and M_2 and separation a , from equation 2.159, the gravitational wave frequency f_r is given by

$$G(M_1 + M_2) = \pi^2 f_r^2 a^3. \quad (2.206)$$

The average flux over source orientations and orbital phases at earth is

$$S = \frac{P}{4\pi r^2} = \frac{P}{4\pi d_L^2} = \frac{P}{4\pi d_M^2(1+z)^2}. \quad (2.207)$$

Inserting for P from equation 2.175, we can re-write the above equation as

$$S = \frac{32c^5}{5G} \left(\frac{GM_c \omega_{gw}}{2c^3} \right)^{10/3} \frac{1}{4\pi d_M^2(1+z)^2}. \quad (2.208)$$

From equation 2.165 we can show

$$M_c = \frac{(M_1 M_2)^{3/5}}{(M_1 + M_2)^{1/5}}. \quad (2.209)$$

Replacing this with M_c from 2.208

$$S = \frac{32c^5}{5G} \left(\frac{G(M_1 M_2)^{3/5} \omega_{gw}}{2c^3(M_1 + M_2)^{1/5}} \right)^{10/3} \frac{1}{4\pi d_M^2(1+z)^2}. \quad (2.210)$$

Now, using equation 2.206, we get

$$S = \frac{\pi c^3}{10G} \left(\frac{4G^2 M_1 M_2}{c^4 a d_M} \right)^2 \left(\frac{f_r}{1+z} \right)^2 = \frac{L_{gw}}{d_L^2} = \frac{L_{gw}}{(1+z)^2 d_M^2}. \quad (2.211)$$

On the right-hand side, the Luminosity per solid angle is averaged over the source orientations (4π).

Similar to the previous section, $\#$ is the total number of events per comoving volume. Hence, the event rate per comoving volume (\dot{N}) is defined as

$$\dot{N} = \frac{d\#}{dt}. \quad (2.212)$$

We introduce the space density $N(a)da$ as the number of systems with separations between a and $a + da$ per comoving volume, we can write

$$N(a) = -\frac{d\#}{da}. \quad (2.213)$$

The minus sign is due to the fact that with decreasing a from infinity, the number of systems increases. Starting with the above equation

$$N(a) = -\frac{d\#}{da} = -\frac{d\#}{dt} \frac{dt}{da} = -\frac{\dot{N}}{\dot{a}}. \quad (2.214)$$

In the last equality, we used the definition in 2.212. On the other hand, the conservation of energy for the binary system with circular orbits states that the change of orbital energy over time is radiated away in the form of gravitational waves, hence

$$L_{gw} = \frac{d}{dt} \frac{GM_1 M_2}{2a} \rightarrow \dot{a} = -\frac{2a^2 L_{gw}}{GM_1 M_2}, \quad (2.215)$$

which, using 2.214, gives

$$N(a) = \dot{N} \frac{GM_1 M_2}{2a^2 L_{gw}}. \quad (2.216)$$

To derive an equation for the number density $N(f_r)df_r$ of sources radiating with a frequency between f_r and df_r , we first note that $N(f_r)df_r = -N(a)da$. Using the above equation

$$N(f_r) = -N(a) \frac{da}{df_r} = -\dot{N} \frac{GM_1 M_2}{2a^2 L_{gw}} \frac{da}{df_r}. \quad (2.217)$$

To replace da/df_r , starting with 2.206, we get

$$\frac{da}{df_r} = -\frac{2}{3} a^{5/2} \sqrt{\frac{\pi^2}{G(M_1 + M_2)}}. \quad (2.218)$$

Inserting for luminosity from equation 2.211, and using the above equation to replace da/df_r

$$N(f_r) = \dot{N} \frac{5c^2}{24G^2 M_1 M_2 f_r^2} a^{5/2} \sqrt{\left(\frac{\pi^2}{G(M_1 + M_2)}\right)}. \quad (2.219)$$

Using equation 2.206 again, in the above equation we can replace a in favor of f_r to get

$$N(f_r) = \dot{N} \frac{5c^2}{24G^2 (M_1 M_2) f_r^2} \left(\frac{G(M_1 + M_2)}{\pi^2 f_r^2} \right)^{5/6} \sqrt{\frac{1}{G(M_1 + M_2)}}, \quad (2.220)$$

which after inserting for M_c from equation 2.209 gives

$$N(f_r) = \frac{5\pi^2}{24} \frac{c^5}{(GM_c)^{5/3}} \frac{\dot{N}}{(\pi f_r)^{11/3}}. \quad (2.221)$$

Hence, the specific intensity (flux per solid angle per frequency bandwidth) of the gravitational waves from sources between z and $z + dz$ is

$$dI = S.N(f_r) \frac{dV_{com}}{d\Omega dz} \frac{df_r}{df} dz. \quad (2.222)$$

To understand this equation, note that, since $N(f_r)df_r$ is the number density in $(f_r, f_r + df_r)$, $SN(f_r)df_r dV_{com}$ is the total flux (with dV_{com} the differential comoving volume). Now dividing the total flux by solid angle $d\Omega$, observed frequency df and redshift dz , gives the flux per solid angle, per observed frequency, per redshift; this is the above equation. Integrating dI over all redshifts gives the total specific intensity

$$I = \int_0^\infty SN(f_r) \frac{dV_{com}}{d\Omega dz} \frac{df_r}{df} dz. \quad (2.223)$$

Inserting for S from the right hand side of equation 2.211, and replacing $N(f_r)$ using the left hand side of equation 2.217 gives

$$I = \int_0^\infty \frac{L_{gw}}{(1+z)^2 d_M^2} \frac{-N(a)da}{df_r} \frac{dV_{com}}{d\Omega dz} \frac{df_r}{df} dz. \quad (2.224)$$

Using equation 2.216 to replace $N(a)$ gives

$$I = \int_0^\infty \frac{L_{gw}}{(1+z)^2 d_M^2} \dot{N} \frac{GM_1 M_2}{2a^2 L_{gw}} \frac{-da}{df_r} \frac{dV_{com}}{d\Omega dz} \frac{df_r}{df} dz. \quad (2.225)$$

Recalling that $df_r/df = 1+z$, and using $1/4\pi$ equation 2.198 to replace $dV_{com}/d\Omega dz$, we get

$$I = \int_0^\infty \frac{L_{gw}}{(1+z)^2 d_M^2} \dot{N} \frac{GM_1 M_2}{2a^2 L_{gw}} \frac{-da}{df_r} \frac{c}{H_0} d_M^2 \frac{1}{E(z)} (1+z) dz, \quad (2.226)$$

with $E(z)$ from equation 2.199. Now, noting that

$$\frac{dt_r}{dz} = \frac{1}{H_0(1+z)E(z)}, \quad (2.227)$$

we can simplify the equation 2.226 to write

$$I = \frac{1}{4\pi} \int_0^\infty c \left(\dot{N} \frac{dt}{dz} \right) \frac{GM_1 M_2}{2a^2} \frac{-da}{df_r} dz. \quad (2.228)$$

The quantity in parenthesis is $N(z)$.

Radiative energy density is related to the total specific intensity (I) via

$$\epsilon_{gw} = \Omega_{gw} \rho_c c^2 = \frac{1}{c} \int I d\Omega = \frac{4\pi}{c} I. \quad (2.229)$$

If we define $\Omega_{gw}(f)$ as the scaled ($1/\rho_c c^2$) energy density per logarithmic frequency, we have $\Omega_{gw} = \Omega_{gw}(f)/f$. Inserting this in the above equation

$$\Omega_{gw}(f) \rho_c c^2 = \frac{4\pi f}{c} I. \quad (2.230)$$

Inserting for I from 2.228, we get

$$\Omega_{gw}(f) \rho_c c^2 = \int_0^\infty N(z) \frac{f}{f_r} \frac{GM_1 M_2}{2a} \left(\frac{-d \ln a}{d \ln f_r} \right) dz. \quad (2.231)$$

Using $f = f_r/(1+z)$ gives

$$\Omega_{gw}(f) \rho_c c^2 = \int_0^\infty \frac{N(z)}{1+z} \frac{GM_1 M_2}{2a} \left(\frac{-d \ln a}{d \ln f_r} \right) dz. \quad (2.232)$$

We can replace a , using equation 2.206 to get

$$\Omega_{gw}(f) \rho_c c^2 = \frac{2}{3} \int_0^\infty \frac{N(z)}{1+z} \frac{GM_1 M_2}{2} \left[\frac{\pi^2 f_r^2}{G(M_1 + M_2)} \right]^{1/3} dz \quad (2.233)$$

$$= \frac{\pi^{2/3}}{3} \frac{(GM_c)^{5/3}}{G} f^{2/3} \int_0^\infty \frac{N(z) dz}{(1+z)^{1/3}}. \quad (2.234)$$

In the second line, we inserted M_c from equation 2.209, and used $f = f_r/(1+z)$. Inserting $\rho_c = 3H_0^2/(8\pi G)$ for critical density, the above equation gives

$$\Omega_{gw}(f) = \frac{8\pi^{5/3}}{9} \frac{1}{c^2 H_0^2} (GM_c)^{5/3} f^{2/3} \int_0^\infty \frac{N(z) dz}{(1+z)^{1/3}} \quad (2.235)$$

Defining N_0 and $\langle (1+z)^{-1/3} \rangle$ as

$$N_0 = \int_0^\infty N(z) dz \quad (2.236)$$

$$\langle (1+z)^{-1/3} \rangle = \frac{1}{N_0} \int_{z_{min}}^{z_{max}} \frac{N(z)}{(1+z)^{1/3}} dz \quad (2.237)$$

We can rewrite equation 2.235 as

$$\Omega_{gw}(f) = \frac{8\pi^{5/3}}{9} \frac{1}{c^2 H_0^2} (GM_c)^{5/3} f^{2/3} N_0 \langle (1+z)^{-1/3} \rangle \quad (2.238)$$

The characteristic strain is related to the energy density via

$$\rho_c c^2 \Omega_{gw}(f) = \frac{\pi c^2}{4G} f^2 h_c^2(f). \quad (2.239)$$

Hence, we can write the equation 2.238 as

$$h_c^2(f) = \frac{4}{3\pi^{1/3} c^2} \frac{(GM_c)^{5/3}}{f^{4/3}} N_0 \langle (1+z)^{-1/3} \rangle. \quad (2.240)$$

This is the equation for the characteristic strain of the stochastic GW background from a cosmic distribution of black hole binaries. Each binary contributes to the total stochastic background via the above equation. In the methods chapter, we will show how, in practice, one can integrate over all the binaries to obtain the stochastic background for the whole distribution.

Semi-Analytic Models

Black Holes are very simple objects, in the sense that we can use three parameters to describe them: mass, spin, and charge. However, for the case of massive astrophysical black holes, the charge is negligible. Hence, the main characteristics describing the Massive Black Holes (MBH) and determining their evolution is their mass and spin (Barausse, 2012; Klein et al., 2016). Accretion from the interstellar medium and mergers of the MBHs can change their mass and spin; the evolution of the host galaxy derives such processes. Therefore, the evolution of MBHs is entangled to the evolution of their host galaxy (Benson, 2010; Silk & Mamon, 2012). Strong observational evidence, such as the tight correlation between the mass of supermassive black holes (SMBHB) and the velocity dispersion of their host bulges (Ferrarese & Merritt, 2000), supports this coupled evolution as well. The subject of this chapter is describing the galaxy formation and evolution models used to predict the cosmic distribution of SMBHBs, their merger rate, and consequently, as discussed in the previous chapter, the stochastic GW background.

3.1 Galaxy/SMBH Coevolution Models

We can follow the evolution of galaxies along with the coevolution of their MBHs through the Eulerian and smoothed-particle hydrodynamical simulations (e.g. EAGLE: Schaye et al. (2015)), and the semi-analytical galaxy formation models (e.g. Barausse (2012); Dayal et al. (2019)).

Solving the equations of motion computationally, allows the hydrodynamical simulations to follow the full dynamical and hydrodynamical evolution of the systems. Due to computational limitations, these sim-

ulations have limited resolution (determined by the least massive particles in simulations). Sub-resolution models allow to include additional physical processes like star formation and supernova feedback. Despite the limited resolution, hydrodynamical simulations provide a better resolution and a better realization of the smaller scale physics, compared to the semi-analytical models. However, for a long time, hydrodynamical models lacked a self-consistent treatment of the sub-grid phenomena such as the star formation, feedback mechanisms, and also the horizon-scale phenomena of MBHs, which determines important aspects of their cosmic evolution, such as their mergers and accretion. Very recently, there have been reports of self-consistent MBH horizon-scale treatment in hydrodynamical simulations (Siwek et al., 2020); however, these models are in general computationally expensive, and hence only cover a small fraction of the galaxy and MBH coevolution parameter space.

On the other hand, the computationally convenient semi-analytic models approximate the star formation, gas physics, and feedback (e.g. supernova) processes with simplified recipes and prescriptions by calibrating the free parameters against the observations. Despite the lack of resolution compared to hydrodynamical simulations, the computational convenience resulted from these simplified prescriptions allows for a wide coverage of the MBH and galaxy evolution parameter space. Hence, since we have a limited understanding of the exact physics of the cosmic evolution of MBHs, we use semi-analytic models for investigating and comparing different plausible models against the observations. As mentioned, the most crucial aspect of such practice is our freedom in spanning the parameter space of MBH evolution, which will play a key role in identifying and constraining the correct model(s).

In this work, we rely on SMBH population realizations in (Klein et al., 2016), which are based on the semi-analytic galaxy formation model introduced in Barausse (2012), and improved in Sesana et al. (2014) and Antonini et al. (2015a,b). Barausse (2012) adopts the extended Press-Schechter formalism of Cole et al. (2002) and Parkinson et al. (2007) to reproduce the statistical properties of the dark matter merger trees in N-body simulations of Springel et al. (2005) and Cole et al. (2008). Barausse (2012) describes the evolution of dark matter haloes along the branches of these merger trees, and then, employs analytical prescriptions at the nodes of the tree to replicate the effects of mergers in evolving the baryonic components. Following the prescription of Taffoni et al. (2003), Barausse (2012) also accounts for the environmental effects such as dynamical friction, tidal-stripping, and tidal evaporation, which we will discuss shortly when we give a more detailed description of the mergers.

Consequently, by accounting for the gas in galactic nuclei, Barausse (2012) can follow the mass and spin evolution of MBHs during the mergers and accretion, along the branches of the merger tree. The merger of two branches of the merger tree indicates merging dark matter haloes and eventually merging the galaxy they contain; this, although with a delay, results in the merger of MBHs that the galaxies host. Regarding the accretion, the amount of gas at the nuclear region determines the spin and accretion rate for the MBH evolution. Barausse (2012) uses the reservoir model of Granato et al. (2004) and Dotti & Ruszkowski (2010) to describe the gas in the nuclear region and account for its feedback on the structure growth through accretion-powered jets. Barausse (2012) considers two categories of accretion: gas-rich and gas-poor nuclear environment. In the gas-rich case, nuclear cold gas accretes on the MBH coherently and as a result, increases the spin of MBH (Bardeen, 1970; Thorne, 1974; Dotti & Ruszkowski, 2010; Maio et al., 2013). In the gas-poor nuclear region, MBH accretes chaotically, with a random distribution of the orbital angular momentum of the in-falling lumps of matter; hence decreasing the MBH spin (King & Pringle, 2006).

Barausse (2012) considered two types of seeds for the MBHs: light and heavy. In the light-seed scenario ($M_{seed} \sim 150M_{\odot}$), MBHs form as the remnants of Pop III stars as discussed in Madau & Rees (2001); for this case, Barausse (2012) starts the merger trees at $z = 20$. In the heavy-seed scenario ($M_{seed} \sim 10^5 M_{\odot}$), Barausse (2012) assumes the MBHs to form from the collapse of massive protogalactic disks (Koushiappas et al., 2004; Lodato & Natarajan, 2006; Begelman et al., 2006); Barausse (2012) starts the merger trees for these seeds at $10 < z < 15$.

The above choice of MBH seeds is motivated by the observation of luminous (bigger than $10^{-47} \text{ergs}^{-1}$) high redshift quasars ($6 < z$); at least some of these quasars are powered by MBHs, which is an implication of the existence of MBHs with masses exceeding $10^9 M_{\odot}$ as early as when the Universe was only 1 Gyr old (Fan et al., 2001). The mechanism responsible for such growth in a short time-span is still an open question (Shapiro, 2005; Volonteri & Rees, 2006; Tanaka & Haiman, 2009; Volonteri, 2010). Numerical simulations of the fragmentation of primordial clouds based on standard cold dark matter (CDM) theories predict very massive first-generation stars (Pop III) (Bromm et al., 2002; Maio et al., 2010) with masses ranging up to several hundred solar masses. The remnant of the collapse of such massive stars (if not supernova), can be massive black hole seeds ranging from tens to several hundred solar masses. These light MBH seeds from the remnants of the first generation stars (Pop III) at $z = 20$ require very high accretion and merger rates to grow to $10^9 M_{\odot}$ by $z = 6$.

Also, during the mergers, large kicks from gravitational-radiation induced recoil can eject these remnants from the proto-galaxies (Tanaka & Haiman, 2009). Hence, the plausibility of light MBH seeds governing the SMBH evolution is questionable (Tanaka & Haiman, 2009; Volonteri, 2010).

Another mechanism for describing the observation of high luminosity quasars at $z = 6$, is assuming an early formation of massive ("heavy", $10^4 - 10^5 M_\odot$) BH seeds ($z \sim 15$), from the direct collapse of the pre-galactic haloes (Begelman et al., 2006; Agarwal et al., 2012). Runaway dynamical instabilities can cause a rapid loss of angular momentum in the self-gravitating gas of pre-galactic haloes. Losing angular momentum leads to an early formation of a compact, self-gravitating core, which further contracts by the continued gas infall. Gas pressure supports this core, and a radiation-dominated envelope surrounds it. Core contraction drastically increases the temperature, leading to cooling via thermal neutrino emission, which consequently results in the formation and rapid growth of a central black hole (Begelman et al., 2006). Despite the plausibility of this model in accounting for the existence of SMBHs at $z = 6$, the underlying mechanism is not well-understood. Current observational evidence is not sufficient to distinguish between the two MBH seed prescriptions discussed above. As is the subject of this work, LISA will enable to carry such discrimination.

Furthermore, alongside the MBH seed prescription, there is another parameter of the galaxy formation models that changes through the SMBH population realizations in Klein et al. (2016), which is the delay between the galaxy and MBH merger. After two dark matter haloes merge, their galaxies crawl to the centre of the newly-formed halo by dynamical friction. Tidal evaporation and tidal stripping removes mass from the smaller galaxy and further evolves the system to merge the galaxies (Lacey & Cole, 1993; Toomre, 1977; Volonteri et al., 2003; Barausse, 2012). After the galaxies merger, dynamical friction against the stellar background drags the MBHs that they host close to each other to form a bound system. This bound state hardens through their three-body interactions with stars, galaxy rotation, and planet-like migration (Begelman et al., 1980; Vasiliev et al., 2014, 2015). At the sub-parsec separations, GW radiation starts to dominate the energy loss of the system, and, as mentioned before, triggers the inspiral of the binary and its eventual merger.

3.2 Merger Event Rates

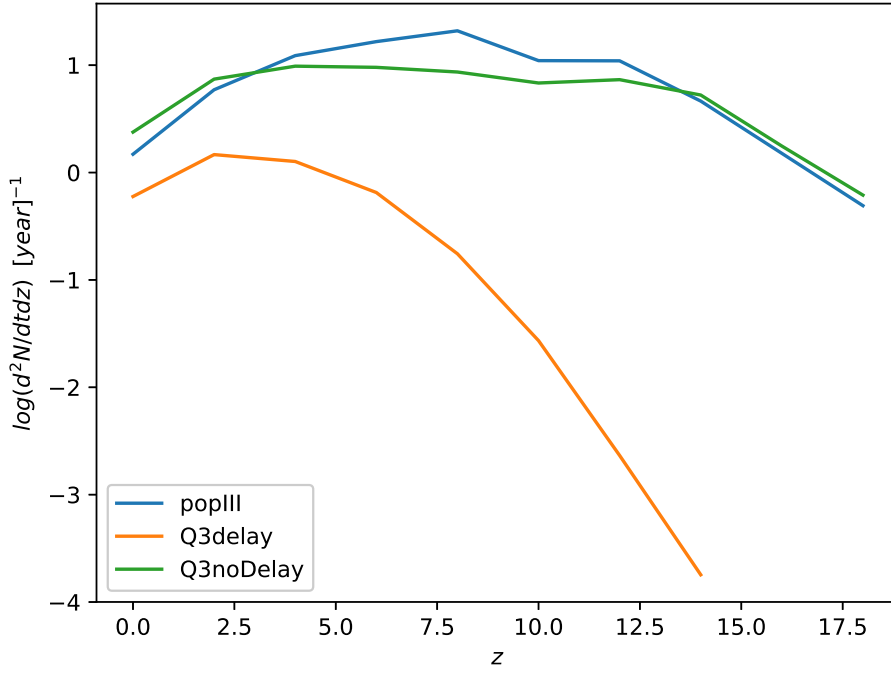


Figure 3.1: comoving rate of SMBHB mergers per unit redshift, per year, plotted against the redshift, for 3 SMBHB population synthesis models of Klein et al. (2016).

As mentioned earlier, the aim of this work is to investigate our ability to use the stochastic GW background in LISA frequency range to distinguish between the three different supermassive black hole population synthesis models introduced in Klein et al. (2016). Here, we give a brief description of these three models; a detailed description is available in (Klein et al., 2016). As mentioned above, these models are SMBHB population realizations from the semi-analytic galaxy formation model of Barausse (2012), with different prescriptions, especially varying in the choice of massive black hole seeds and the delay between the galaxy and MBH mergers. Different choices of seed and delay, result different SMBHB populations: (1) Pop III: this model starts with light mass seeds from Pop III stars, and also accounts for the delay between the massive black holes and galaxy mergers. (2) Q3 delay: this model starts with heavy mass seeds from the collapse of protogalactic disks, and similar to the first model, accounts for

the delay between the massive black holes and galaxy mergers. (3) Q3 no delay: similar to the second model, but does not correct for the delay between the massive black hole and galaxy mergers. Each model is characterized by the distribution of comoving number density of SMBHBs over the mass of the black hole components (m_1, m_2) and their redshift (z).

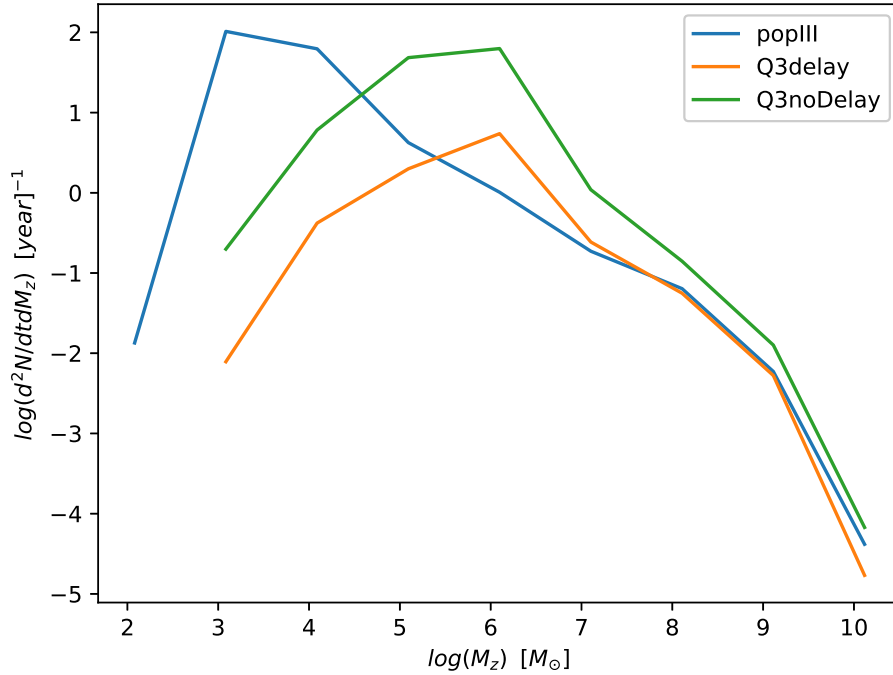


Figure 3.2: comoving rate of SMBHB mergers per logarithmic redshifted mass ($M_z = (1+z)M_{total}$), per year, plotted against the redshifted mass (M_z) for 3 SMBHB population synthesis models of Klein et al. (2016).

We use

$$\frac{d^2N}{dzdt} = 4\pi c N_{com}(z) \left(\frac{d_L(z)}{(1+z)} \right)^2 [yr^{-1}] \quad (3.1)$$

to calculate the number density of mergers (merger event rate) per unit redshift, per unit time (yr^{-1}). $d_L(z)$ is the luminosity distance at z and $N_{com}(z)$ is the comoving number density of binaries in the redshift range z and $z + dz$. Calculating $N_{com}(z)$ requires integration over all the possible masses, at each redshift (z). Figure 3.1 shows the merger event rate per

unit redshift, per unit time, for three realizations of SMBHB populations introduced in Klein et al. (2016).

Similarly, we can calculate the number of events per redshifted total-mass ($M_z = M(1 + z)$), per unit time, using

$$\frac{d^2N}{dM_z dt} = 4\pi c N_{com}(M_z) \left(\frac{d_L(z)}{(1+z)} \right)^2 [yr^{-1}]. \quad (3.2)$$

Figure 3.2 shows the merger event rate per logarithmic redshifted mass, per unit time, for three SMBHB models introduced in Klein et al. (2016).

Methods

Throughout this work, we will investigate and develop mechanisms to distinguish between various realizations of Supermassive Black Hole Binary (SMBHB) populations from the semi-analytic galaxy formation models available in the literature. For the purposes of this work, as an introduction to such methods, it is sufficient to assess our discrimination capabilities on a handful of SMBHB population realizations. However, the extension of these methods to include a more complete sample of semi-analytic galaxy formation models and SMBHB population realizations therein is rather straightforward. We will document the fundamentals of such extension along the way and will elaborate on it with more details in the discussion section.

This chapter aims to act as a standalone methods section, enabling readers to reproduce the formalisms we used to distinguish between the various realizations of SMBHB populations of Klein et al. (2016). The first section will briefly describe our algorithm for calculating the stochastic gravitational-wave (GW) background from a SMBHB population. In the second section, we will introduce the Hierarchical Bayesian Statistics, which, in the third section, we will employ to distinguish between SMBHB population synthesis models, by using the stochastic GW background. In section 4, we introduce a complementary technique by adding the data from the individually resolved SMBHB mergers to improve our ability in distinguishing between SMBHB population synthesis models. In section 5, we will introduce our sampling algorithm to recover the population of SMBHBs from the stochastic GW background and investigate its consistency with the results of Hierarchical approach.

4.1 Calculating the Stochastic GW Background

Section 2.4 gives a brief introduction on calculating the stochastic gravitational wave signal from a population of massive black hole binaries. First, we recall the equation 2.240, originally introduced by Phinney (2001)

$$h_c^2(f) = \frac{4}{3\pi^{1/3}c^2} \frac{(GM_c)^{5/3}}{f^{4/3}} N_0(1+z)^{-1/3}. \quad (4.1)$$

This equation gives the characteristic strain of the stochastic GW background in frequency f . Recalling from section 3.2, a population of SMB-HBs is characterized by the co-moving number density of mergers per mass and redshift: $N_0(m_1, m_2, z)$, in which m_1 and m_2 are the masses of the first and second binary components. Hence, we can rewrite the equation 4.1 as

$$h_c^2(f, m_1, m_2, z) = \frac{4}{3\pi^{1/3}c^2} \frac{(GM_c)^{5/3}}{f^{4/3}} N_0(m_1, m_2, z)(1+z)^{-1/3}. \quad (4.2)$$

Besides, recalling from section 2.4, each merger emits gravitational-waves in a limited frequency range (f_{min}, f_{max}). As the distance between the binaries shrinks, the frequency of the gravitational-wave emission increases. We can determine the minimum emission frequency (f_{min}) by the maximum distance between the two components of the binary. From Kepler's law, we can measure the orbital frequency of the binary in its rest-frame

$$\omega_{s,rest}^2 = \frac{GM_{rest}}{a_{rest}^3}, \quad (4.3)$$

where a_{rest} is the rest-frame separation, and M_{rest} is the rest-frame total mass. Hence, since $\omega_s = 2\pi f_s$ and $f_{gw} = 2f_s$, and taking the maximum rest-frame separation of the two components to be 1pc , it is easy to show that

$$f_{gw,rest,min} = \frac{100}{6.308\pi} \frac{1}{\sqrt{G(m_1 + m_2)}}, \quad (4.4)$$

where $f_{gw,rest,min}$ is the minimum frequency of the emitted gravitational-wave. Now, we can rewrite the above equation for the observed minimum frequency of the gravitational-wave emission (f_{min})

$$f_{min} = \frac{100}{6.308\pi} \frac{1}{(1+z)} \frac{1}{\sqrt{G(m_1 + m_2)}}. \quad (4.5)$$

Similarly, we can calculate the maximum frequency (f_{max}) from the minimum separation between the two components of the binary. In a Schwarzschild geometry, there is a minimum radial distance between the components, below which, circular orbits are no longer allowed; this is called the Innermost Circular Orbit (ISCO). In the rest-frame of the binary

$$r_{ISCO} = \frac{6GM}{c^2}, \quad (4.6)$$

where again M is the total mass ($m_1 + m_2$). Replacing the separation a_{rest} in equation 4.3 with 4.6, and using $\omega_s = 2\pi f_s$ and $f_{gw} = 2f_s$, and also $f_{obs} = f_{rest}/(1+z)$, we can derive the maximum frequency of the emitted GW in the observer frame

$$f_{max} = \frac{1}{6\sqrt{6}\pi} \frac{1}{(1+z)} \frac{c^3}{3.154 \times 10^7} \frac{1}{G(m_1 + m_2)}. \quad (4.7)$$

As mentioned above, each merger, radiates gravitational-waves in a limited range of frequency (f_{min}, f_{max}), determined by 4.5 and 4.7. Therefore, given a population of SMBH mergers, each one of them contributes to the total stochastic GW background in a limited frequency range. In other words, in each frequency, a limited subset of the whole population of SMBH mergers contributes to the stochastic background. To determine if a specific merger, characterize by mass (m_1, m_2) and redshift (z) contributes to the stochastic background in a given frequency, it suffices to calculate (f_{min}, f_{max}) from equations 4.5 and 4.7; if $f \in (f_{min}, f_{max})$, this merger contributes to the background in that frequency (f). Hence, we can rewrite the equation 4.2 as

$$h_c^2(f) = \sum_z \sum_{m_1, m_2} \frac{4}{3\pi^{1/3}c^2} \frac{(GM_c)^{5/3}}{f^{4/3}} N_0(m_1, m_2, z)(1+z)^{-1/3} \quad (4.8)$$

where $N_0(m_1, m_2, z) = 0$ if $f(m_1, m_2, z) > f_{max}$ or $f(m_1, m_2, z) < f_{min}$. Using equation 4.8 we can calculate the stochastic GW background.

4.2 Hierarchical Bayesian Approach

This section is a brief introduction on Hierarchical Bayesian statistics, as a reference for what follows throughout the rest of this chapter. In essence, Hierarchical Bayesian Statistics is very similar to the Bayesian Statistics, and we can summarize their main difference in one word: parameters.

We will briefly recall the familiar concept of Bayesian statistics, and build on its simple definitions to introduce the Hierarchical Bayesian approach. In what follows, we heavily rely on Thrane & Talbot (2019) as an introductory reference for the subject.

4.2.1 Bayesian Statistics

Recalling from any basic master-level course on statistics, in Bayesian Statistics we are interested in calculating the posterior probability distribution function (PDF) of the parameter, given the data,

$$p(\theta|\vec{d}) = \frac{\mathcal{L}(\vec{d}|\theta)\pi(\theta)}{\mathcal{Z}}, \quad (4.9)$$

where $p(\theta|\vec{d})$ is the posterior PDF of the parameter θ given the data (\vec{d}) , $\mathcal{L}(\vec{d}|\theta)$ is the likelihood of the data, given the parameter. $\pi(\theta)$ is the prior information for the parameter, and \mathcal{Z} is the evidence acting as a normalization constant. Therefore

$$\mathcal{Z} \equiv \int d\theta \mathcal{L}(\vec{d}|\theta)\pi(\theta), \quad (4.10)$$

and with this definition

$$\int d\theta p(\theta|\vec{d}) = 1. \quad (4.11)$$

The prior information contains our knowledge and constraints on the parameter before running the experiment. We can calculate the likelihood from the corresponding likelihood function. For example, in case of a Gaussian noise, we can replace the likelihood with the Gaussian likelihood

$$\mathcal{L}(\vec{d}|\theta) = \frac{1}{2\pi\sigma^2} \exp\left(-\frac{1}{2} \frac{|\vec{d} - \vec{\mu}(\theta)|^2}{\sigma^2}\right), \quad (4.12)$$

where σ is the uncertainty, and $\vec{\mu}(\theta)$ represents our theoretical prediction for the data, for θ .

In case of a multi-parameter model, it suffices to integrate over the irrelevant parameter to get the posterior PDF of the parameters of interest. In other words, we marginalize over the uninteresting parameters to get the posterior PDF of the parameters we want:

$$p(\theta_i|\vec{d}) = \int \left(\prod_{k \neq i} d\theta_k \right) p(\theta|\vec{d}) = \frac{\mathcal{L}(\vec{d}|\theta_i)\pi(\theta_i)}{\mathcal{Z}} \quad (4.13)$$

where

$$\mathcal{L}(\vec{d}|\theta_i) = \int \left(\prod_{k \neq i} d\theta_k \right) \pi(\theta_k) \mathcal{L}(\vec{d}|\theta). \quad (4.14)$$

4.2.2 The Odds

Now, to take one step toward introducing the Hierarchical Bayesian Statistics, we will introduce the evidence ratios and odds. If we have two models A and B with parameters θ_A and θ_B , the evidence for these models is defined as (from the evidence defined in equation 4.10)

$$\mathcal{Z}_A \equiv \int d\theta_A \mathcal{L}(\vec{d}|\theta_A) \pi(\theta_A) \quad (4.15)$$

and

$$\mathcal{Z}_B \equiv \int d\theta_B \mathcal{L}(\vec{d}|\theta_B) \pi(\theta_B). \quad (4.16)$$

We can write the evidence ratio as

$$BF_B^A = \frac{\mathcal{Z}_A}{\mathcal{Z}_B}, \quad (4.17)$$

which from now on, we will call the A/B Bayes Factor. For example, in the case at hand, A and B can be two different SMBHB population realizations from a galaxy formation model, each having their own parameters. Here, as discussed in 3.2, since we describe each population by the distribution of SMBHBs over the total-mass and redshift spaces, these parameters are the same set of parameters ($\{\theta_A\} = \{\theta_B\}$). Hence, we can take the number density of SMBHBs per total-mass bin ($d^2N/dMdt$), and the number density of SMBHBs per redshift bin ($d^2N/dzdt$) as our model parameters. The Bayes factor, as defined above, measures the ratio of the evidence of the model A over the model B .

However, instead of the Bayes Factor, the correct metric to compare the two models is the "odds", defined as

$$O_B^A = \frac{\mathcal{Z}_A \pi_A}{\mathcal{Z}_B \pi_B}, \quad (4.18)$$

Where π_A (π_B) is our prior information on model A (B) before running the experiment. The odds provides a framework to compare different models (rather than their intrinsic parameters) against the data \vec{d} . As promised, this is a step forward in comparing different galaxy formation (and SMBHB population realizations) models directly against the data.

4.2.3 Hierarchical Bayesian Statistics

Now we will continue upon these definitions by introducing the Hierarchical Bayesian Statistics. We emphasize that this section serves as an introduction to the Hierarchical Bayesian Statistics, and we refer the interested reader to Thrane & Talbot (2019).

First, we will generalize our priors to account for the different models as well as different parameters. We can define a new prior as

$$\pi(\theta|\Lambda), \quad (4.19)$$

in which, as before, θ is the intrinsic model parameter. Λ is called the hyper-parameter, which goes through the different models. For example, for our purposes, Λ is a hyper-parameter from the discrete parameter space containing different galaxy formation models and the unique SMBHB population realizations based on them. Hence, the above prior gives the prior information for the parameter (θ), given that Λ is the correct model. Hence it is normalized

$$\int d\theta \pi(\theta|\Lambda) = 1. \quad (4.20)$$

What we are interested in is calculating the posterior PDF of the hyper-parameter Λ , given the data \vec{d} . Hence, we define the hyper-posterior as

$$p(\Lambda|d) = \frac{\mathcal{L}(d|\Lambda)\pi(\Lambda)}{\int d\Lambda \mathcal{L}(d|\Lambda)\pi(\Lambda)}, \quad (4.21)$$

where the denominator, similar to the Bayesian posterior is only a normalization constant. $p(\Lambda|d)$ is the posterior PDF of the hyper-parameters given the data, and $\pi(\Lambda)$ is our prior belief of the hyper-parameter (Λ) before running the experiment. To emphasize on the difference between

this prior and the prior defined in 4.19 above, $\pi(\Lambda)$ is our prior belief on the models (Λ) before conducting the experiment, whereas $\pi(\theta|\Lambda)$ is our prior belief on θ , an intrinsic parameter for the Λ model, given that Λ is the only available model. The likelihood $\mathcal{L}(d|\Lambda)$ is defined similarly to the Bayesian likelihood

$$\mathcal{L}(d|\Lambda) = \int d\theta \mathcal{L}(d|\theta) \pi(\theta|\Lambda). \quad (4.22)$$

The only difference between this likelihood and the one used in Bayesian posterior PDF is that here we integrate over the intrinsic-parameter space for each model Λ . Recalling from the derivation of the 4.13 above, it is easy to see that, such integration (marginalization) over the intrinsic parameters is necessary, since we are not interested in the posterior PDF of the intrinsic-parameters, but rather the posterior PDF of the hyper-parameters.

We can also generalize this definition to multiple hyper-parameters, by following a similar prescription to what we used to derive the equation 4.13. However, in this work hyper-parameter space is a discrete one-dimensional space, we will not need such generalization.

4.3 Hierarchical Bayesian Statistics in this Work

This section is a follow-up to the brief introduction we gave in the previous section on the Hierarchical Bayesian Statistics. We will build upon the basic concepts of the previous section to specialize in the application of Hierarchical Bayesian Statistics in our work: **using the stochastic GW background to distinguish between different realizations of SMBHB populations**

Before anything, it is crucial to note that the observables of SMBHB mergers in a gravitational-wave survey fall under two main categories: (1) the stochastic GW background and (2) the individually resolved SMBHBs. In this section, we will focus on applying the Hierarchical Bayesian formalism to the stochastic GW background. In the next sections, we will also include the individually resolved binaries to improve our analysis.

4.3.1 Hierarchical Framework

We are interested in distinguishing between different semi-analytic galaxy formation models, constraining the “most likely” model and the most likely SMBHB population realization therein. Following the methods introduced in the previous section, we marginalize over the mass and redshift distributions and compare the models directly against each other. Recalling the posterior PDF for Hierarchical Bayesian statistics from equation 4.21

$$p(\Lambda|\vec{d}) = \frac{\mathcal{L}(\vec{d}|\Lambda)\pi(\Lambda)}{\int d\Lambda \mathcal{L}(\vec{d}|\Lambda)\pi(\Lambda)} \quad (4.23)$$

in which we called the posterior, hyper-posterior. Λ is the hyperparameter, which in our case is a simple labelling parameter, corresponding to the different SMBHB population synthesis models under study. Hence, for the example of using SMBHB population realizations from Klein et al. (2016), $\Lambda = \{1, 2, 3\}$, corresponding to Pop III, Q3 delay, and Q3 no delay, respectively. \vec{d} is the data vector, which is the observed stochastic GW background by a gravitational-wave instrument (e.g. LISA and Decigo). $\pi(\Lambda)$ is the hyper prior, which includes our prior information on the hyperparameter, which we will calculate in the next section from the individually resolved binaries, and for simplicity consider it to be flat here. The denominator is the hyper-evidence, which we will treat as a normalization constant throughout this work.

The hyper-posterior described above, by definition, is what we need to compare different galaxy formation models and SMBHB realizations based on them, against an observed stochastic GW background. We will develop the necessary tools for calculating the hyper-posterior throughout this section. To emphasize where the marginalization lies, we note that by going from $p(d^2N/dzdt, d^2N/dMdt|\vec{d})$ to $p(\Lambda|\vec{d})$, our parameters changed from the mass and redshift distribution of the SMBHBs to the labeling parameter Λ .

Renaming $(d^2N/dzdt)$ and $(d^2N/dMdt)$ by ψ_z and ψ_m , respectively, we can use equation 4.24 to write

$$\mathcal{L}(\vec{d}|\Lambda) = \int d\psi_z d\psi_m \mathcal{L}(\vec{d}|\psi_z, \psi_m) \pi(\psi_z, \psi_m|\Lambda), \quad (4.24)$$

where $\mathcal{L}(\vec{d}|\psi_z, \psi_m)$ is the likelihood of the data, given that ψ_m and ψ_z describe the mass and redshift distributions of SMBHBs. Following from the definition 4.19, $\pi(\psi_z, \psi_m|\Lambda)$ is our prior information for ψ_m and ψ_z given a fixed SMBHB population realization (labeled by Λ here). It is easy to see that $\pi(\psi_z, \psi_m|\Lambda)$ denotes the information from the simulations; in other terms, what is the likelihood of this specific mass and redshift distribution (ψ_z, ψ_m) for the SMBHBs, given the “ Λ ” SMBHB population synthesis model?

Equation 4.24 is a straightforward marginalization over the mass and redshift distributions. The challenging part is calculating the likelihood, which is computationally expensive. This is indeed the likelihood of the observed stochastic GW background for each possible combination of mass and redshift distribution of the SMBHBs; in practice, this is an infinite-dimensional parameters space.

The data is the strain ($S_O(f)$) of the observed stochastic GW background over the frequency range of the instrument. Since we have the mass and redshift distribution of the mergers directly from the simulations, we can simplify the above integration as follows. Each unique mass and redshift distribution of SMBHBs binaries results in a unique stochastic background signal. We can calculate this signal for each simulation (which we did in section 2.4). Comparing this predicted signal from simulations with the observed signal is equivalent to the above likelihood. To show this, if we take the above prior ($\pi(\psi_z, \psi_m|\Lambda)$) to be a delta function, excluding any mass and redshift distribution other than the ones predicted by the given simulations, the integral reduces to an integral over the frequency space. We call this likelihood the strain likelihood and denote it by

\mathcal{L}_S from now on

$$\mathcal{L}_S(\vec{d}|\Lambda) = \int df \mathcal{L} \left[S_O(f) | (\psi_z, \psi_m)_\Lambda \right], \quad (4.25)$$

where, as before, Λ (or the hyper-parameter) is one of the labels 1,2,3 for our three SMBHB realizations from Klein et al. (2016). We can rewrite this likelihood by noting that each mass-redshift distribution predicts a unique stochastic GW background signal $S_\Lambda(f)$. Hence 4.26 is equivalent to

$$\mathcal{L}_S(\vec{d}|\Lambda) = \int df \mathcal{L}(S_O(f) | S_\Lambda(f)). \quad (4.26)$$

Equation 4.26 is what we use as the “likelihood” throughout the rest of this work to compare different realizations of SMBHB population directly against the stochastic GW background.

4.3.2 Posterior Distribution

We know that the posterior PDF of the hyper-parameter (models), given the data, is given by equation 4.26. Here, we will detail the practical and computational approach that we used to calculate the posterior PDF. To avoid any confusion, we should again mention that the prior $p(\Lambda)$ in equation 4.23 is taken to be flat for now, which is why we are allowed to call equation 4.26 the posterior PDF. We will also add the prior information in the next section, and multiply this likelihood with it to get a more sophisticated posterior PDF.

We can write the likelihood in equation 4.26 in terms of a Gaussian chi-squared and its probability

$$\chi^2(\Lambda) = \sum_f \frac{(S_O(f) - S_\Lambda(f))^2}{\sigma(f)^2}, \quad (4.27)$$

in which σ is the instrument error which itself can be a function of frequency. The probability corresponding to chi-squared is given by

$$L_S(\vec{d}|\Lambda) = \exp \left[-\frac{\chi^2(\Lambda)}{2} \right]. \quad (4.28)$$

As discussed before, in the case of a flat prior, this equation gives the probability of each model (Λ), given the observed stochastic GW background. We need to mention that, the choice of the chi-squared function above,

corresponding to a Gaussian distribution, is justified as long as the instrument error is a Gaussian scatter around the true stochastic GW background. Throughout this work, we simulate the observed stochastic GW background by adding Gaussian scatter to the prediction of SMBHB population synthesis models. Hence, the above choice of chi-squared function is in accordance with the errors of our "observed" stochastic GW background.

4.4 Individually Resolved Binaries

The previous section shows our method for deriving the likelihood of each SMBHB population realization directly from the observed stochastic GW background. The reliability of the results and our ability in distinguishing between different galaxy formation models depends on the observation noise; increasing the noise will weaken the constraints derived from the stochastic GW background. Moreover, by increasing the number of models under study, degeneracies in the hyper-parameter space will start to appear, which also will further increase by increasing the observation noise.

The intuitive way to handle these complications is inserting the prior information in equation 4.23. Recalling this equation, we derived the likelihood part in the previous section and postponed deriving the prior to this section. Our strategy is to use the individually resolve SMBHB mergers to derive the hyper-priors in equation 4.23. This is the subject of this section.

4.4.1 Signal to Noise Ratio

Before describing our method for deriving the priors from the individually resolved binaries, we have to clarify one definition. We can calculate the strain for merging SMBHBs by equations 2.184 and 2.185. Dividing this strain by the sensitivity line of our instrument, if the ratio between the two is larger than 5, we accept this event as a high signal-to-noise ratio event. We expect such events to be individually resolved by the corresponding instrument.

4.4.2 Deriving the Priors

Before introducing our method, it is important to emphasize that in this section we are not interested in the total number of individually resolved binaries by a GW survey, but rather, the prior derived from their mass and redshift distribution. In fact, the total number of individually resolved binaries is one of the highly anticipated SMBHB population observables for discriminating between different models (Tanaka & Haiman, 2009; Volonteri, 2010), but, as previously discussed, the aim of this work is to investigate alternatives to the total-number of resolved binaries.

We are interested in deriving the prior from the observations of indi-

vidually resolved binaries (\vec{d}_r)

$$\pi(\Lambda) = \pi(\Lambda|\vec{d}_r) = \mathcal{L}(\Lambda|\vec{d}_r), \quad (4.29)$$

the second equality is emphasizing that we derive this prior from the observations of individually resolved binaries, and independent from the stochastic GW background.

Dividing the total-mass and redshift spaces to a finite number of bins, for each SMBHB population synthesis model, we can assign a probability to each bin, defined as the probability of having an individually resolvable merger in that bin. This is simply the normalized number density of individually resolvable mergers per unit time per mass-redshift bin, predicted by a given SMBHB population synthesis model. By normalized, we mean that summing the normalized number of individually resolvable mergers per bin, over all bins, is equal to one. Denoting the normalized number of individually resolvable mergers from the model Λ , in the i 'th mass-redshift bin by $\mathcal{N}_{\Lambda,i}$ we can define the chi-squared as

$$\chi_\pi^2(\Lambda) = \sum_i \frac{(\mathcal{N}_{O,i} - \mathcal{N}_{\Lambda,i})^2}{\mathcal{N}_{\Lambda,i}}, \quad (4.30)$$

where i goes through all the mass-redshift bins, and $\mathcal{N}_{O,i}$ is the normalized number of "observed" individually resolvable mergers in the i 'th mass-redshift bin. From this, we can write the likelihood

$$\pi(\Lambda) = \mathcal{L}(\Lambda|\vec{d}_r) = \exp\left[-\frac{\chi_\pi^2(\Lambda)}{2}\right]. \quad (4.31)$$

Hence, having a sample of observed individually resolved binaries from a GW survey, it suffices to know which mass-redshift bin any given binary belongs to. Then, using equation 4.30, we can derive a prior from this sample to include in our posterior PDF calculation in equation 4.21, and hence improve our capability to distinguish between different realizations of SMBHB populations.

Since sky-localization for the high-redshift merger is difficult, we expect large uncertainties on their derived mass and redshifts. Hence, we can not assume knowing the mass and redshift of all individually resolved binaries. However, we can optimize the above approach to account for this, by considering wide mass-redshift bins; this allows us to use a weaker constraint on the mass and redshift of the resolved binaries, since in equation 4.30 we only assume knowing the corresponding mass-redshift bin for an individually resolved binary, rather than its exact mass and redshift.

In this work, as documented in the results section, we divided the mass-redshift space to 100 bins (10 bins in the redshift and 10 bins in the mass directions). However, we expect to modify this choice in a more careful treatment; we will discuss this in more detail in the discussion section.

4.5 Recovering the SMBHB Population

In section 5.1, we introduced our methods for calculating the stochastic GW background from a SMBHB population, and using it alongside the individually resolved binaries to discriminate between such populations, realized from semi-analytic galaxy formation models. In this section, we will introduce our algorithm for recovering the SMBHB population from the stochastic GW background. Comparing the recovered SMBHB population with the predicted population from SMBHB population synthesis models provides a standalone method for discriminating between the models. Moreover, comparing the recovered population of SMBHBs (by the methods of this section), with the predicted population of the distinguished (by the Hierarchical method) SMBHB population synthesis model, allows for check of consistency between the two methods.

Throughout this work, at first, we will limit ourselves to the stochastic background in LISA frequency range, to assess our ability in recovering the SMBHB population by relying on a single GW instrument. Then, we will also include the stochastic GW background in Decigo frequency range, in order to improve the recovered constraints for the population of SMBHBs. This section is an introduction on our MCMC approach, and we present the results of employing these methods in section 5.4.

4.5.1 MCMC Sampling

Recalling from section 2.4, we can calculate the stochastic background using equation 4.8, and by imposing the frequency condition given there. It would be straightforward to use a Markov Chain Monte Carlo (MCMC) sampler to use this equation for sampling the underlying SMBHB population for any stochastic background.

We have different realizations of the SMBHB populations from different semi-analytic galaxy formation model (namely, those of Klein et al. (2016)). Each realization of SMBHB population corresponds to a unique stochastic GW background (section 2.4). Since the comparison of the distribution of SMBHBs in redshift and total-mass spaces with the realized population from simulations will enable us to distinguish between different galaxy formation and SMBHBs population synthesis models, it suffices to recover the SMBHB distribution separately in redshift space and total-mass space.

Starting with the mass space, above translates to using a given stochastic GW background to recover the distribution of SMBHBs over the total mass of the binary. As mentioned before, this recovery is possible through

MCMC sampling. To implement this, we sample for the number density of SMBHBs in each mass over the range of the possible total-masses of the binary, to recover the stochastic GW background.

The main complication, however, is the "dimensionality". The total-mass of the binary ranges from a couple of hundreds to 10^{10} solar masses. Sampling for all the points in the total-mass space is not possible. As mentioned above, we want to sample for the number density of the binaries as a function of the total mass. However, this sentence is phrased in a way that one might think recovering the number density over a continuous range of total mass is an option. To be clear, we need one sampler (and hence, one dimension) for each point of the total-mass space that we want to recover its number density. Therefore, probing a continuous range in the total-mass space requires an infinite-dimensional sampler.

To resolve this infinite-dimensionality problem, we divide the space of total-mass of the binary into equal bins, and will instead, sample for the number density of the SMBHBs in each one of these bins, to recover the stochastic GW background. On the other hand, using the same bins, by integrating over the redshift space, we can predict the number of SMBHBs that we can expect in each bin from each one of the SMBHB population synthesis models.

Comparing the sampled number density in each bin against the expected number density from the models enables us to distinguish between the different models using an "observed" stochastic GW background. To carry such comparison, we use

$$\chi_{i,M}^2 = \sum_{M_j} \frac{\left((d^2N/dM_j dt)_{\text{sampling}} - (d^2N/dM_j dt)_i \right)^2}{(d^2N/dM_j dt)_i}. \quad (4.32)$$

Where $\chi_{i,M}^2$ denotes the chi-squared derived by comparing the recovered distribution of SMBHBs with the expected distribution from the i 'th simulation (subscript M reminds us that we are comparing the recovered populations in the mass space). $(d^2N/dM_j dt)_{\text{sampling}}$ is the median of the sampled number densities in the j 'th mass bin. $(d^2N/dM_j dt)_i$ is the expected number density from the i 'th SMBHB population synthesis model in the j 'th mass bin. The integration (summation) is over all the mass bins; in other words, M_j goes through the (binned) total-mass space. The probability defined from this chi-squared ($p = \exp(-\chi_{i,M}^2/2)$) has a simple interpretation: it is the probability of the i 'th model being responsible for the given stochastic GW background.

We can follow a similar approach for the redshift distribution of the SMBHBs. We divide the redshift space into equal bins, and sample for the number density of the SMBHBs in each redshift bin. Similar to equation 4.32 we can write

$$\chi_{i,z}^2 = \sum_{z_j} \frac{\left((d^2N/dz_jdt)_{\text{sampling}} - (d^2N/dz_jdt)_i \right)^2}{(d^2N/dz_jdt)_i}. \quad (4.33)$$

Here, $\chi_{i,z}^2$ denotes the chi-squared of the comparison between the recovered distribution of the SMBHBs over redshift bins with the expected distribution from the i 'th SMBHB population synthesis model. We denote the median of the sampled number densities in the j 'th redshift bin by $(d^2N/dz_jdt)_{\text{sampling}}$; $(d^2N/dz_jdt)_i$ is the expected number density from the i 'th model, for the j 'th redshift bin. Similar to the equation for the total-mass space, integration (summation) is over the redshift space, going through all the redshift bins.

Finally, we note that in order to calculate $(d^2N/dM_jdt)_i$, it suffices to integrate over the redshift space in each mass bin to get the "total number of SMBHBs in that mass bin"; similar applies to the case of redshift space. Multiplying the probabilities calculated in $\chi_{i,z}^2$ and $\chi_{i,M}^2$, gives the joint constraints on the SMBHB population synthesis models, using the combined mass and redshift distributions.

Results

In the previous section, we introduced our methods for 1) calculating the stochastic gravitational-wave (GW) background from a given population of supermassive black hole binaries (SMBHB), 2) employing the Hierarchical Bayesian statistics to distinguish between different SMBHB population synthesis models using the stochastic GW background, and how to improve the results by including the data from the individually resolved mergers, and 3) recovering the distribution of SMBHBs from the stochastic GW background, and checking its consistency with the results of the Hierarchical approach. In this section, we will apply these methods on three SMBHB population synthesis models (namely, Pop III, Q3 delay, and Q3 no delay) introduced in Klein et al. (2016), which are based on the semi-analytic galaxy formation model in Barausse (2012), as discussed in section 3.2.

5.1 Stochastic GW Background

Using the methods of section 4.1, we will calculate the stochastic GW background predicted by the SMBHB population synthesis models in Klein et al. (2016) and Dayal et al. (2019), in the LISA and Decigo frequency ranges. Including the SMBHB population synthesis models of Dayal et al. (2019) in this section, is for the purpose of a quick comparison, and we will not study these models further in this work. Recalling from section 4.1, for the characteristic strain of the stochastic GW background, we have

$$h_c^2(f) = \sum_z \sum_{m_1, m_2} \frac{4}{3\pi^{1/3}c^2} \frac{(GM_c)^{5/3}}{(f(m_1, m_2, z))^{4/3}} N_0(m_1, m_2, z)(1+z)^{-1/3}, \quad (5.1)$$

where $N_0(m_1, m_2, z) = 0$ if $f(m_1, m_2, z) > f_{max}$ or $f(m_1, m_2, z) < f_{min}$.

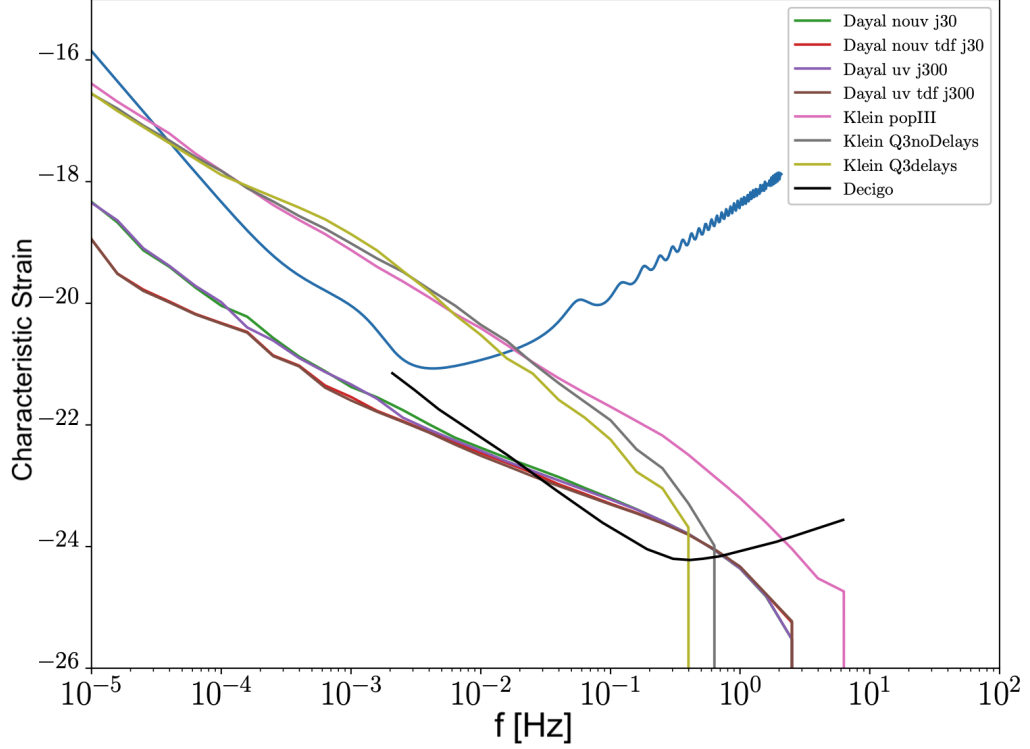


Figure 5.1: predicted stochastic GW background by the SMBHB population realizations from two different galaxy formation models introduced in Dayal et al. (2019) and Barausse (2012). Including 4 models from Dayal et al. (2019): nouv j30, nouv tdf, uv j300, and uv tdf j300 (green, red, purple, and brown lines, respectively), and 3 models from Klein et al. (2016): Pop III, Q3 delay, and Q3 no delay (pink, grey, and yellow lines, respectively). The dark-blue line shows the sensitivity lines of LISA, and the black line shows the sensitivity line of Decigo.

The predicted population by each SMBHB population synthesis model is characterized by the distribution of the comoving number of mergers over the mass and redshift: $N_0(m_1, m_2, z)$. Hence, it is straightforward to insert the populations from Klein et al. (2016) and Dayal et al. (2019) in the above equation. Figure 5.1 shows the resulting characteristic strain for the stochastic GW background; it shows the stochastic background calculated from the four models in Dayal et al. (2019): nouv j30, nouv tdf, uv j300, and uv tdf j300, and three models in Klein et al. (2016): Pop III, Q3 delay, and Q3 no delay. We plotted the stochastic background against the sensitivity curves of LISA and Decigo.

Figure 5.1 shows that the SMBHB population synthesis models in Klein et al. (2016) predict stochastic GW backgrounds well-above the sensitivity lines of LISA and Decigo, and hence, detectable by both instruments; whereas, the models in Dayal et al. (2019) predict stochastic backgrounds below the sensitivity line of LISA, and therefore, only detectable by Decigo.

5.2 Direct Model Comparison

In the following section, we employ our method of section 4.3 to use the stochastic GW background for distinguishing between different realizations of SMBHB populations in Klein et al. (2016). Throughout this section, we will limit ourselves to only use the stochastic GW background in LISA frequency range. However, it is needless to mention that the same approach also applies to the Decigo or combined (LISA + Decigo) frequencies. As we will discuss in the discussion chapter, to fully assess our capability in distinguishing between such models by using the stochastic GW background, it is straightforward to expand this method to include more galaxy formation models and SMBHB population realizations from them.

5.2.1 Observed Stochastic Background

We want to use the observed stochastic GW background by LISA, to discriminate between different SMBHB population synthesis models. Since such observation is currently unavailable (and will not be till the early 2030s), we will simulate an "observed" stochastic GW signal, to assess our Hierarchical method. To do so, we take the predicted signal by one of the SMBHB population synthesis models, and add a noise model, by adding a Gaussian noise to the strain at each frequency. To produce a realistic noise model, we consider the scatter to be a fraction of the strain ($\log(S_O(f))$) at each frequency, in other words

$$\log(S_O(f)) = \mathcal{G}\left(\log(S_\Lambda(f)), \epsilon \log(S_\Lambda(f))\right), \quad (5.2)$$

in which ϵ is the Gaussian scattering amplitude. To be more precise, the scattering amplitude should be a function of the frequency itself and depends on the instrumental details of LISA and Decigo; such considerations result in a more sophisticated noise model, which we will not (yet) employ in this work. S_O is the observed strain and S_Λ is the predicted strain by the Λ 'th SMBHB population synthesis model. For the current purposes, we fix the Λ . Figure 5.2 shows an observed stochastic GW background, simulated by adding a 2% Gaussian noise ($\epsilon = 2\%$ in equation 5.2) to the Q3 delay SMBHB population synthesis model from Klein et al. (2016). The (currently) accepted frequency range of LISA is above 10^{-4}Hz ; hence, we will not use the stochastic GW background in frequencies below 10^{-4}Hz . We will also ignore the simulated stochastic signal where it falls below the LISA sensitivity curve (which means no detection).

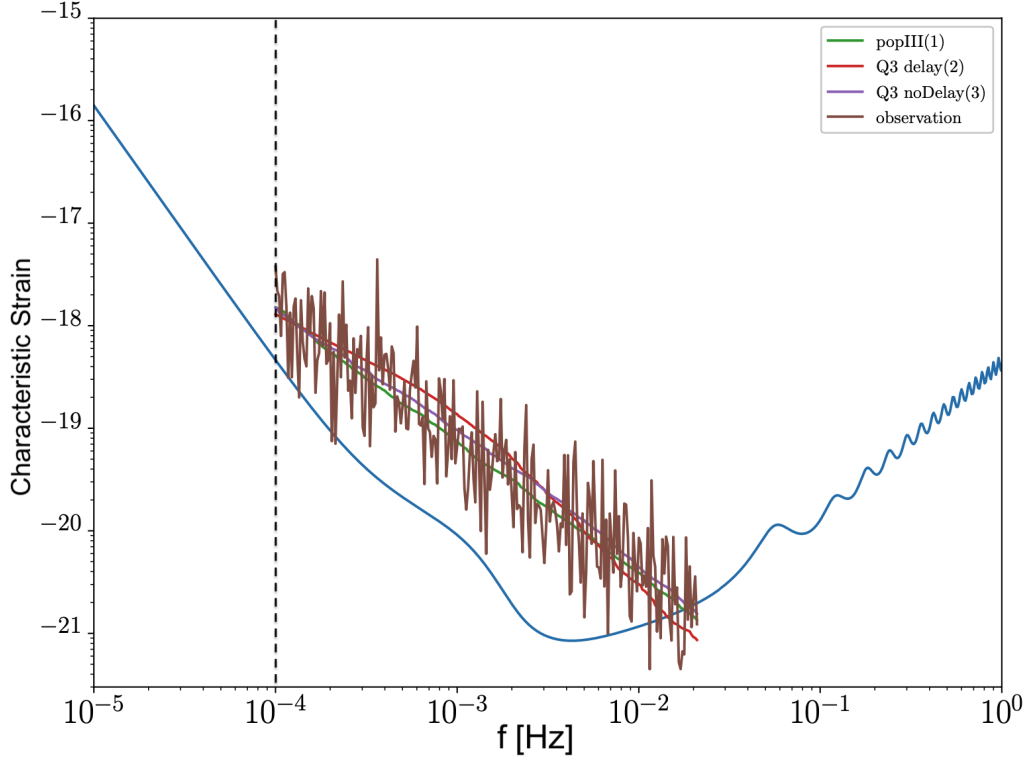


Figure 5.2: our simulation for the observed stochastic gravitational wave background in LISA frequency range, over-plotted on the sensitivity line of LISA. We added 2% logarithmic Gaussian scatter to the Q3 delay SMBHB population synthesis model of Klein et al. (2016). Since the currently accepted frequency range for LISA is larger than 10^{-4} Hz, we will neglect the stochastic GW background in frequencies below 10^{-4} Hz (dashed black line). Also, we will not use the stochastic GW signal where it falls below the sensitivity line of LISA (dark blue line), which corresponds to no detection.

5.2.2 Posterior Distribution

Now that we have an observed stochastic GW signal, using the methods of section 4.3, we can calculate the likelihood of the models ($\Lambda \in$ SMBHB population synthesis models), given by equation 4.26. As we discussed in section 4.3, using equation 4.26 is the same as calculating the posterior distribution in equation 4.24 with a flat prior. We will calculate this prior from the individually resolved binaries in the next section; but throughout this section, we will assume a flat prior.

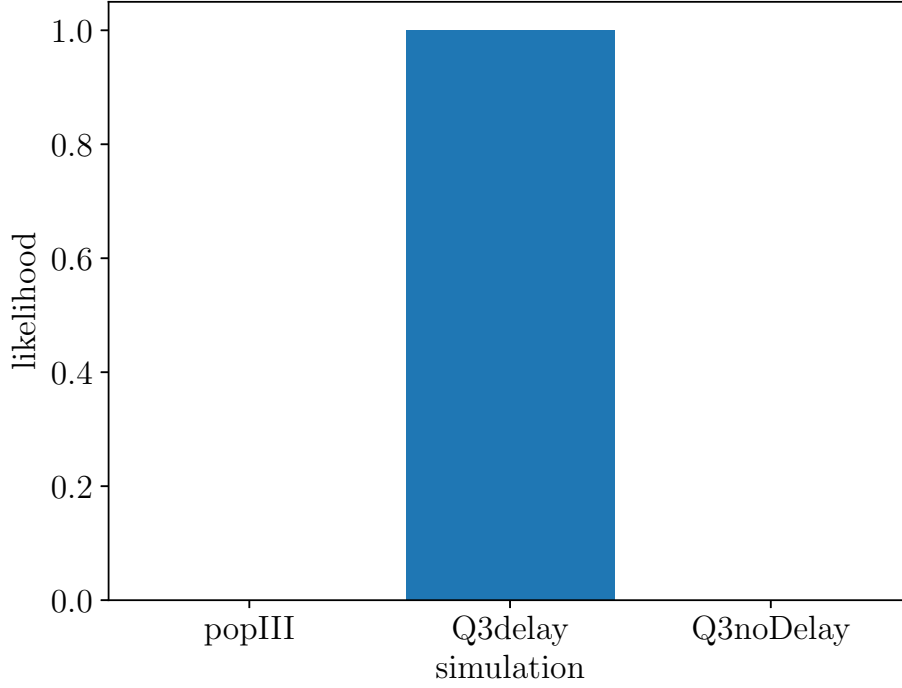


Figure 5.3: constraints on the SMBHB population synthesis models of Klein et al. (2016), derived from the observed stochastic GW signal shown in figure 5.2 (Q3 delay model + 2% noise).

Recalling from equations 4.27 and 4.28, we can calculate the likelihood in equation 4.26 using a Gaussian chi-squared and its probability

$$\chi^2(\Lambda) = \sum_f \frac{(S_O(f) - S_\Lambda(f))^2}{\sigma(f)^2}, \quad (5.3)$$

and

$$L_S(\vec{d}|\Lambda) = \exp\left[-\frac{\chi^2(\Lambda)}{2}\right]. \quad (5.4)$$

$\sigma(f)$ is the instrumentation error (as a function of frequency); in other words, the scatter ($\epsilon \log(S_\Lambda(f))$) used in equation 5.2 to simulate the observations, which itself was a function of frequency.

Taking Λ to be in $\{1, 2, 3\}$ (Pop III, Q3 delay, Q3 no Delay), we have the predicted stochastic GW signal for each model from section 5.1. Hence, we can use the above equations (5.3 and 5.4) to calculate the likelihood

of each model. Figure 5.3 shows the normalized calculated likelihoods for each model, where the observed stochastic GW background is the one shown in figure 5.2: Q3 delay model with 2% Gaussian noise.

With increasing observational noise, we will lose our ability to discriminate between different SMBHB population synthesis models, by only relying on the stochastic GW background. Figure 5.4 shows the constraints on SMBHB population synthesis models, derived from the Q3 delay model with 10% observation noise.

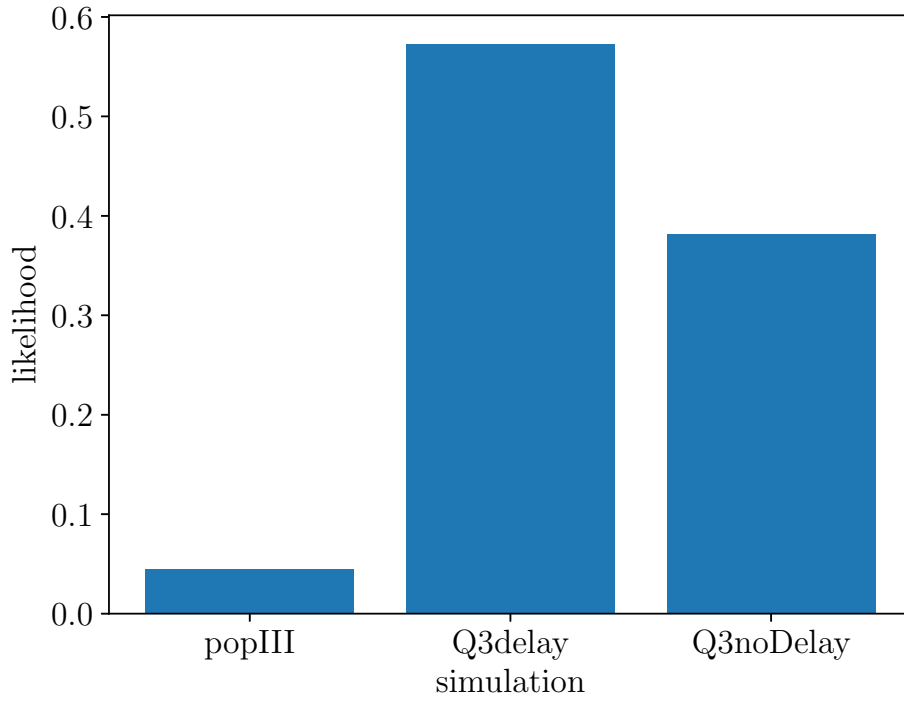


Figure 5.4: constraints on the SMBHB population synthesis models in Klein et al. (2016), derived from an observed stochastic GW signal simulated by adding 10% Gaussian noise to the stochastic signal predicted by Q3 delay model.

5.2.3 Observational Limits

Comparing figures 5.3 and 5.4 shows that increasing the observation noise from 2% to 10% weakens the derived constraints on SMBHB population synthesis models. The subject of this section is to investigate the effect of

observation noise on our ability to distinguish between different SMBHB population synthesis models. The questions that we want to answer is, **what is the observational noise level, below which we would be able to use the stochastic GW background as a standalone source of data to distinguish between the different models of Klein et al. (2016)?** To investigate this, we change ϵ (noise) in equation 5.2 from 0% to 30% and assess our distinguishing abilities at each step.

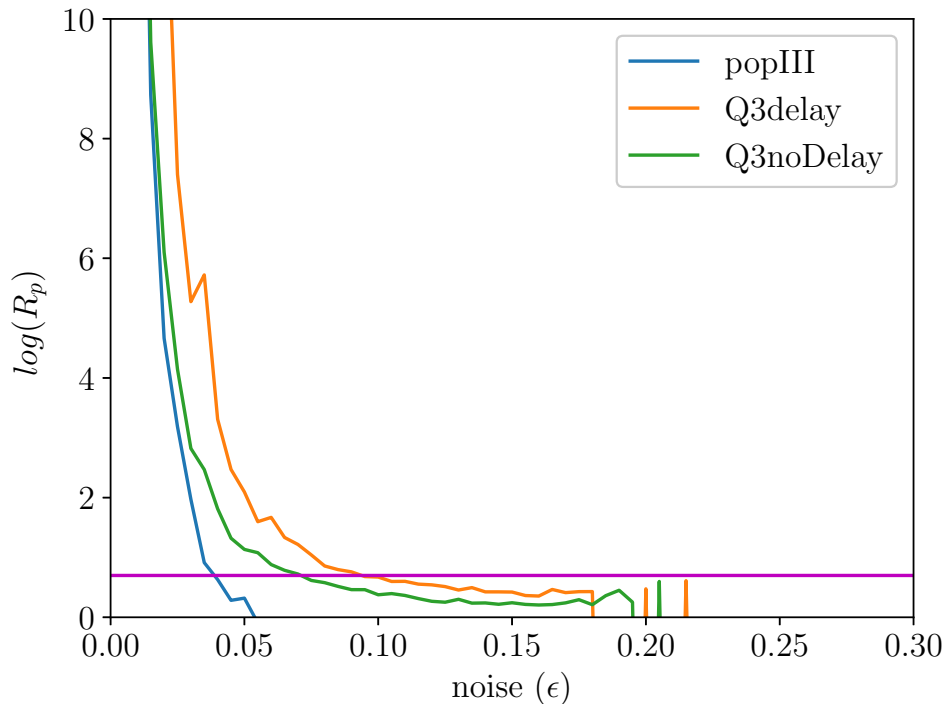


Figure 5.5: probability ratio (R_p , as defined by 5.5) plotted against the observation noise (ϵ , as defined in equation 5.2), for three SMBHB population synthesis models of Klein et al. (2016). Pink line shows the $R_p = 5$ cutoff, excluding the noise levels above which we can not solely rely on the stochastic GW background to distinguish between SMBHB population synthesis models.

We define the probability ratio (R_p) as the likelihood of the true model over the likelihood of the most-likely model amongst the remaining models

$$R_p = \frac{p(\Lambda_{true}|\vec{d})}{\max[p(\Lambda_i|\vec{d})]} \quad \text{where } i \neq \text{true}, \quad (5.5)$$

where Λ_{true} denotes the true model. We can set 5 as a reasonable limit for R_p ; meaning that, if the derived likelihood for the true model is 5 times larger than the second most likely model, we can comfortably distinguish between the true model and the rest of the population synthesis models, solely relying on the stochastic GW background.

We calculated R_p for different noises (ϵ) in the range of 0 to 0.3. To minimize the random nature of the R_p , due to the fact that we derive it from noisy (random) observations, we calculated R_p for 1000 noisy realizations of the observed stochastic GW background at each given noise level (ϵ , refer to equation 5.2), and averaged over them to calculate R_p . Since the predicted stochastic GW background slightly varies among different population synthesis models in Klein et al. (2016), we expected a slightly different behaviour for R_p depending on the model used to simulate the observed stochastic GW background. Figure 5.5 shows R_p plotted against the observation noise (ϵ), for the observed stochastic GW background simulated from the SMBHB population synthesis model in Klein et al. (2016). Defining the "observational limit" as the error (ϵ) at which R_p drops below 5, the observational limit for Pop III, Q3 delay, and Q3 no delay models are 4%, 9.5%, and 7% respectively.

5.3 Individually Resolved Mergers

The previous section shows how to derive the likelihood of each SMBHB population synthesis model, directly from the observed stochastic gravitational wave background, and showed that increasing the observation noise weakens our constraints on the SMBHB population synthesis models. Hence, as shown in figure 5.5, at high enough observation noises ($\sim 10\%$ depending on the true model), we predict to lose our ability to solely rely on the observed stochastic GW background for distinguishing between SMBHB population synthesis models. Moreover, by increasing the number of models under study, we will start to notice degeneracies in the hyper parameter space; such degeneracies will then increase by increasing the observation noise.

One way to handle such complications is investigating another method to constrain the SMBHB population synthesis models, in parallel to using the stochastic GW background. Our suggestion is using the individually resolve mergers of supermassive black hole binaries to derive the hyper-priors in equation 4.23; this is the subject of this section.

5.3.1 Simulating the Observations

Before starting with the formalism of how to derive the priors from the individually resolved binaries, first, we will introduce the model that we used to simulate such observations for LISA. As discussed before, each SMBHB population synthesis model predicts the distribution of the number density of mergers over the mass and redshift spaces. We divide the mass space into equal logarithmic bins, and similarly, we divide the redshift space into equally sized bins. As a result, we can label each resulting bin in the mass-redshift space by two indices: mass and redshift. Using this, we can describe each simulation by its comoving number density of mergers per mass-redshift bin.

Now, to predict the total number of individually resolvable mergers per bin, and in total (by LISA), we use the LISA sensitivity line. We define the signal to noise ratio of a merger, as the ratio of its strain to the sensitivity strain of LISA in that frequency. By LISA, we expect to individually resolve every merger with a signal to noise ratio above 7.0. Therefore, by calculating the signal to noise ratio for each merger event in our SMBHB population, we get the number density of individually resolvable binaries per mass-redshift bin (and also in total, by integrating over all bins). Dividing the number of individually resolvable binaries per mass-redshift bin by the total number of individually resolvable binaries gives the prob-

ability of an individually resolvable merger happening in each bin. Since by definition, the sum of probabilities over all the bins adds up to 1.0, from now on, we will refer to this as the “normalized individually resolvable merger rate” per bin.

Each SMBHB population synthesis model corresponds to a sample of normalized individually resolvable merger rate and a total (over all of the bins) number of individually resolvable mergers per unit time; from the latter, we have the total number of individually resolved mergers for each SMBHB population synthesis model during the three years of LISA operation (N_{total}). Since we know the probability of an individually resolvable merger to happen in each bin (normalized individually resolvable merger rates), to simulate the observations of individually resolved binaries, we draw N_{total} times random realizations of this sample.

Hence, what we have as the simulated observation of individually resolved binaries by LISA, is the number of individually resolved mergers in each bin. To avoid possible confusion in what follows, we need to mention that each individually resolved merger in LISA, produced by this approach, corresponds to a total binary mass and a redshift, coming from the fact we assume knowing its corresponding mass-redshift bin. Moreover, the precision of these corresponding mass and redshift depends on the total number of bins. Increasing (decreasing) the number of bins will increase (decrease) the precision in knowing the mass and redshift of each individually resolved merger.

The simulated observation of individually resolved mergers is a random realization of the normalized merger rate per bin sample. Hence, increasing the assumed period of LISA (which results in a drawing a larger sample), or equivalently, using a SMBHB population synthesis model that predicts more mergers per unit time, results in a more descriptive and complete realization of the data.

As a side note, it will become clear in what follows, that since we used a minimal number of bins (100 bins in total; 10 in mass and 10 in redshift direction), this method (even though it will benefit from) does not rely on a precise mass and redshift estimation of the individually resolved mergers. It suffices to know the corresponding wide bin for each individually resolved mergers in LISA.

5.3.2 Deriving the Priors from Observations

In this section, using the simulated “observation” of individually resolved binaries described above, we will follow the methods of section 4.4.2 to

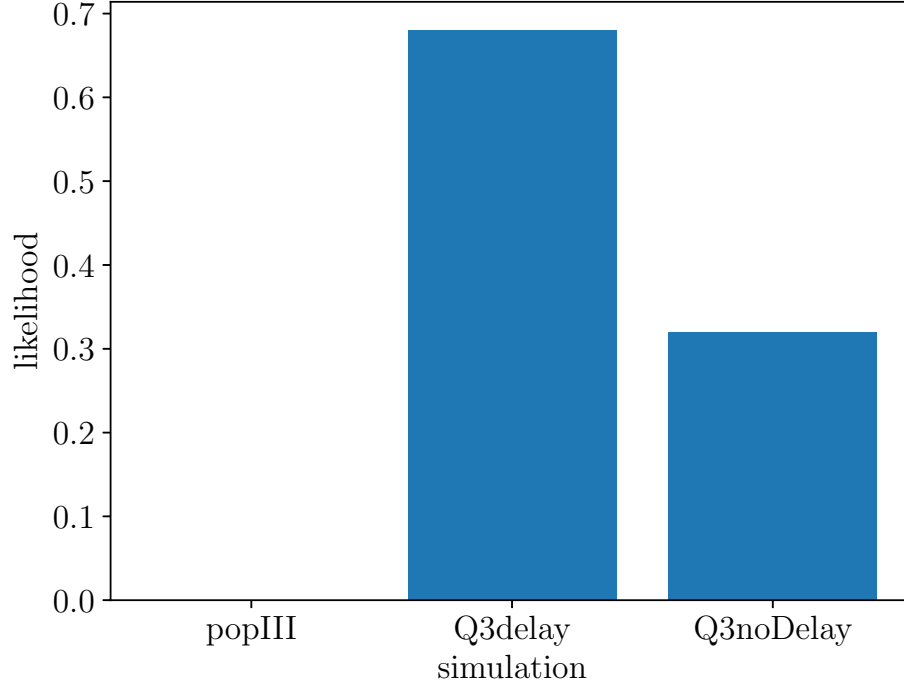


Figure 5.6: constraints on SMBHB population synthesis models of Klein et al. (2016), derived from 20 individually resolved SMBHB merger events, randomly drawn from Q3 delay model.

derive the priors. It is important to emphasize that here we are not interested in the total number of individually resolved binaries by LISA, and will rather derive the prior from the mass and redshift distribution of such events.

As mentioned above, we have the observed number of individually resolved mergers in each mass-redshift. Following the definition (from section 4.4.2) for the normalized number of observed individually resolvable mergers in the i 'th mass-redshift bin ($\mathcal{N}_{O,i}$), we divide the simulated (for LISA) number of individually resolved mergers in each bin by the total number of such events (for LISA). Using equations 4.30 and 4.31, we compare the normalized individually resolved binaries by LISA against the predictions by each SMBHB population synthesis model ($\mathcal{N}_{\Lambda,i}$), to calculate the chi-squared and the prior from the observations. Figure 5.6 shows the prior derived from the individually resolved binaries in 3 years lifespan of LISA. We simulated the observations by drawing 20 random real-

izations from the sample of normalized number of individually resolved mergers per mass-redshift bin (100 bins defined above), predicted by the second model (Q3 delay). 20 individually resolvable binaries is a realistic assumption for the Q3 delay model in the lifespan of LISA.

5.3.3 Joint Constraints

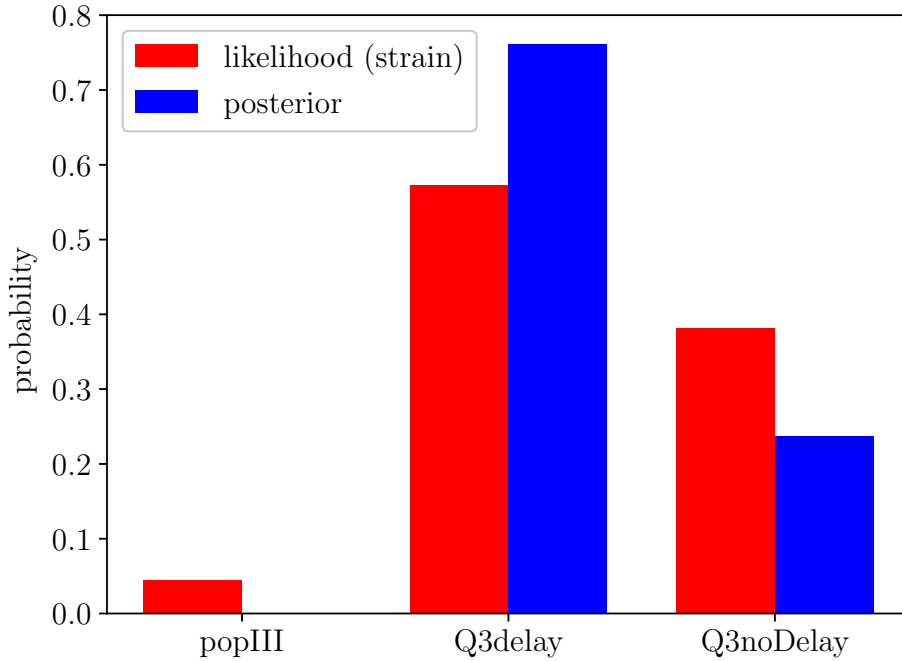


Figure 5.7: red bars: likelihood of each SMBHB population synthesis models, derived from the observed stochastic GW background (simulated from Q3delay model with 10% instrument noise). blue bars: posterior distribution of the SMBHB population synthesis models, derived by multiplying the likelihood with the prior shown in figure 5.6 (from 20 individually resolved binaries of the Q3 delay model).

In previous sections, we calculated the likelihood (from stochastic GW background) and prior (from individually resolved binaries). Recalling equation 4.23, it suffices to multiply the likelihood and prior and renormalize to get the resulting posterior distribution function for the semi-analytic

SMBHB population synthesis models (Λ)

$$p(\Lambda|\vec{d}) = \frac{L(\vec{d}|\Lambda)\pi(\Lambda)}{a_0}, \quad (5.6)$$

where a_0 is a normalization constant. Figures 5.7 shows the likelihood (red), and the posterior PDF (blue) of the SMBHB population synthesis models, derived from a simulated observation of stochastic GW signal in LISA frequency range, with 10% noise, and a simulated observation of 20 individually resolved binaries - both from Q3 delay model. As figure 5.7 indicates, including the priors from individually resolved binaries strengthens our constraints on SMBHB population synthesis models.

5.4 Recovering the Distribution of SMBHBs

In section 4.5, we introduced our MCMC sampling method for recovering the population of SMBHBs from the stochastic GW signal. In this section, we assess our ability to recover the underlying population, from the stochastic signal predicted by SMBHB populations synthesis models of Klein et al. (2016). Section 5.1 shows the stochastic background signal predicted by each model. We will consider one of these stochastic signals as the “observed” signal and attempt to recover its underlying SMBHB population.

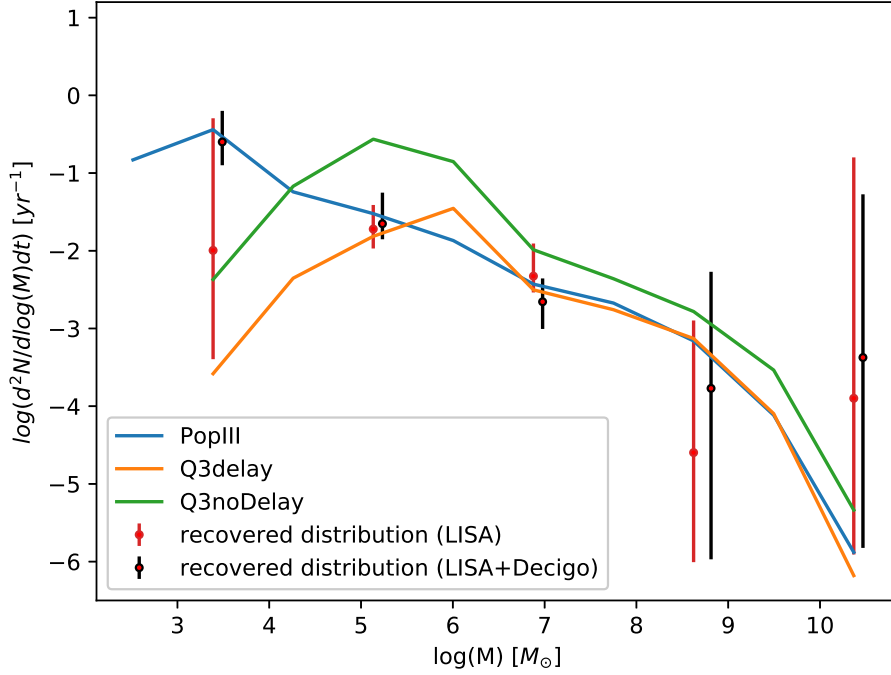


Figure 5.8: First-sigma constraints on the number density of merger events per logarithmic mass, per unit time, derived from the stochastic gravitational wave background predicted by the Pop III model of Klein et al. (2016). The blue, orange, and green lines, respectively show the number densities of the Pop III, Q3 Delay, and Q3 no Delay SMBHB populations synthesis models of Klein et al. (2016). Red (black) error bars show the first-sigma significance of the constraints, derived by sampling from the signal in LISA (LISA + Decigo) frequency range(s).

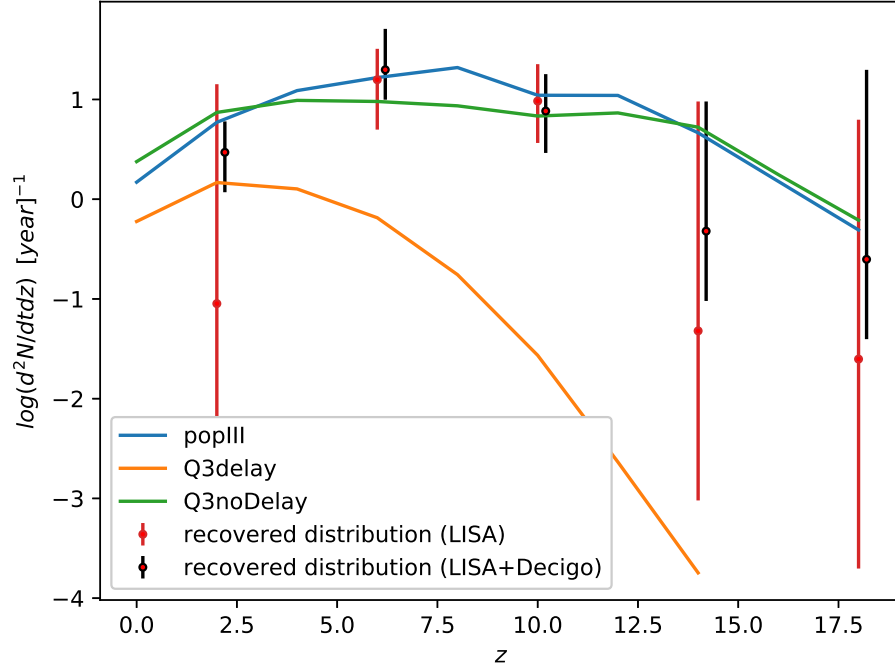


Figure 5.9: First-sigma constraints on the number density of merger events per unit redshift, per unit time, derived from the stochastic gravitational wave background predicted by the Pop III model in Klein et al. (2016). The blue, orange, and green lines, respectively show the number densities of the Pop III, Q3 Delay, and Q3 no Delay MBHB populations synthesis models of Klein et al. (2016). Red (black) error bars show the first-sigma significance of the constraints, derived by sampling from the signal in LISA (LISA + Decigo) frequency range(s).

As mentioned in section 4.5, one of the complications for recovering the population of SMBHBs is the infinite dimensionality of the total-mass and redshift spaces. Starting with the mass space, following our approach there, we divide the space of the total-mass of the binary into five equal bins in the logarithmic scale. It is inevitable that increasing the number of bins will require more computational power, and at the same time, will weaken the derived constraints for each bin.

We used Pop III model to produce the observation. For MCMC sampling, we started with a random initial value in $(0, 1)$ for the number density of merger events per unit logarithmic mass, per unit time, in each bin. Figure 5.8 shows the resulting constraints on the number density of

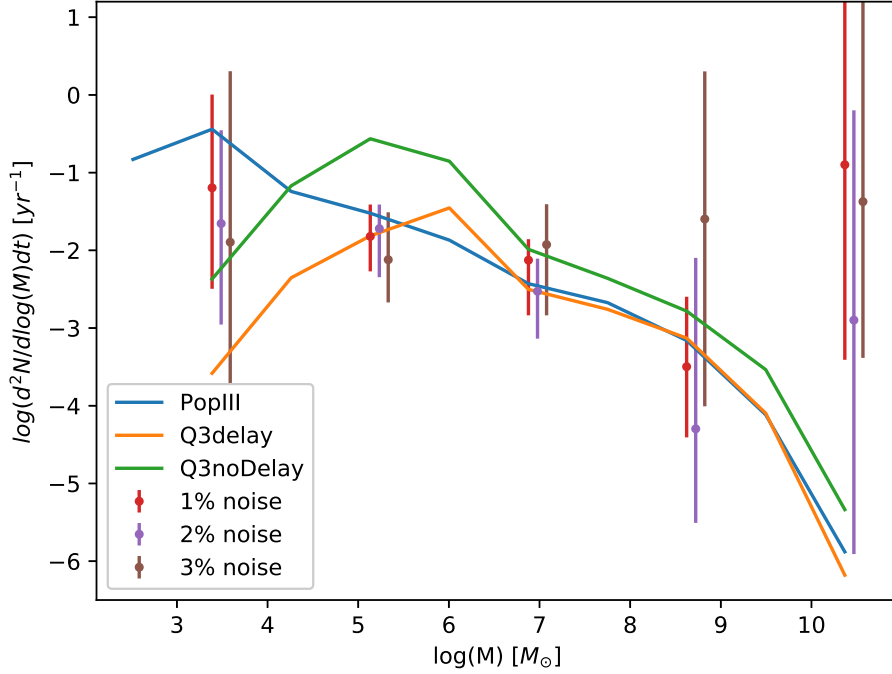


Figure 5.10: First-sigma significance of the constraints on the number density of merger events per logarithmic mass, per unit time, derived from the stochastic gravitational wave background predicted by the Pop III model, in LISA frequency range, with 3 different noise levels: 1%, 2%, and 3%; shown by blue, purple, and brown error bars, respectively.

merger events per unit logarithmic mass, per unit time, derived from the Pop III stochastic GW background in LISA frequency range (10^{-4}Hz , $2 \times 10^{-2}\text{Hz}$). The error bars show the $1\text{-}\sigma$ significance of the constraints. As figure 5.8 shows, by using the stochastic signal in LISA frequency range, we can properly constrain the number density of SMBHB mergers per unit logarithmic mass, per unit time, in the second and third mass bins, which correspond to $10^{6.8}M_{\odot}$ and $10^{8.6}M_{\odot}$. However, our ability to constrain the number density in the lowest mass bin (first bin) and highest mass bins (fourth and fifth bins) by using the stochastic signal in LISA frequency range, is limited, as is apparent by the large uncertainties in recovered number densities in these bins. Constraints of figure 5.8 are the result of a 12-walker MCMC running for 2000 steps, which took approximately 320 hours of CPU time.

For the redshift space, similar to the total-mass space, following the

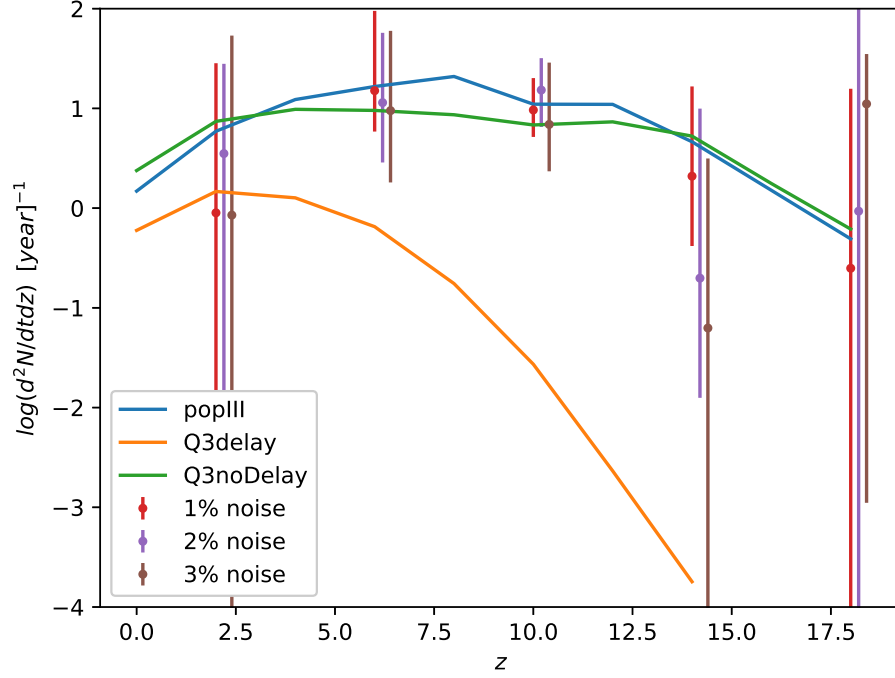


Figure 5.11: First-sigma significance of the constraints on the number density of merger events per unit redshift, per unit time, derived from the stochastic gravitational wave background predicted by the Pop III model, in LISA frequency range, with 3 different noise levels: 1%, 2%, and 3%; shown by blue, purple, brown error bars, respectively.

approach of section 4.5, we divide the space into five equal bins. Again by choosing random initial values in $(0, 1)$ for the number density of mergers per unit redshift, per unit time, and using the Pop III stochastic signal in the LISA frequency range as the observation, we derived the constraints on the number density of mergers per unit redshift, per unit time, in each one of the five redshift bins. Figure 5.9 shows the resulting constraints from, again, 12 walkers, 2000 steps, and 300 hours of CPU time. The error bars are showing the $1\text{-}\sigma$ significance of the constraints. Similar to the total-mass case, we could constrain the second and third bins in the redshift space, by using the stochastic signal in LISA frequency range; but our ability to constrain the lowest and highest redshift bins is limited.

There is a simple approach to improve the recovered constraints on the number density. Instead of using the stochastic background in the LISA frequency range (10^{-4}Hz , $2 \times 10^{-2}\text{Hz}$), we could also include the

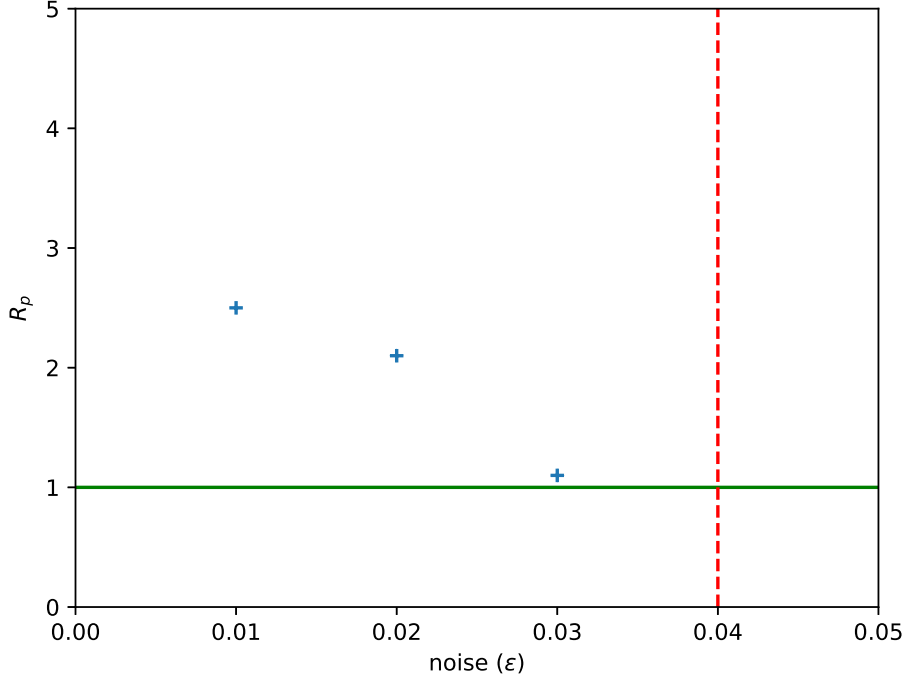


Figure 5.12: probability ratio (R_p) for the SMBHB distribution constraints derived from the stochastic GW background predicted by Pop III model with three noise levels (1%, 2%, and 3%) shown in figures 5.10 and 5.11. Green line shows $R_p = 1$ (below which, we will favor the wrong model as the most likely model). The red-dashed line shows the observational limit for Pop III model (refer to figure 5.5).

stochastic background in the Decigo frequency range (10^{-2}Hz , 10Hz). Figures 5.8 and 5.9 show the improved constraints on the number density of merger events per unit logarithmic mass, per unit time, and the number density of merger events per unit redshift per, unit time, respectively. Comparing the constraints derived from the stochastic GW background in LISA frequency range, and those derived from the combined range of LISA and Decigo (figures 5.8 and 5.9), shows that the most significant improvements are those in the lowest mass and lowest redshift bins.

Thus far, we have not considered any observation noise for the stochastic GW background. From section 5.2.3 and figure 5.5 we know that our observational limit for the case of Pop III model is 4%. To assess our ability in recovering the SMBHB population from a noisy observation, we add (following the method of section 5.2.1) three different levels of noise (1%,

2%, and 3%) below the observational limit, to the stochastic signal of Pop III model, and employ our MCMC algorithm to recover the distribution of SMBHBs from these noisy observations. Figure 5.10 (5.11) shows the recovered constraints on the number density of mergers per mass (redshift) bin.

Finally, we multiply the probabilities from equations 4.32 and 4.33 to use the recovered distributions in figure 5.10 and 5.11 for distinguishing between the SMBHB population synthesis models. Figure 5.12 shows the probability ratio (R_p , as defined by equation 5.5) for the noise levels (and the resulted constraints) of figures 5.10 and 5.11 (1%, 2%, and 3%). The red line in figure 5.12 indicate where $R_p = 1$; if for a given noise, R_p falls below this line, we will not identify the true model as the most likely model for the given stochastic background and hence, we will lose consistency with the results of the Hierarchical approach. Figure 5.12 shows that as long as the noise is below the observation limit (figure 5.5), we can recover the distribution of SMBHBs in consistence with the constraints derived from the Hierarchical approach.

Discussion

This work presents an unprecedented attempt at using the stochastic gravitational wave background as the focal point to discriminate between different supermassive black hole binary population synthesis models. Despite that these SMBHB population synthesis models are drawn from the same semi-analytic galaxy formation model, the expansion of this work to include various semi-analytic galaxy formation models is straightforward. Which is because the main mechanism remains intact, and it suffices to have a prediction for the stochastic gravitational-wave background from each new SMBHB population realization (from any given galaxy formation model). Hence, ultimately, this work is showcasing the potential of using the upcoming detection of stochastic GW background to discriminate between various semi-analytical galaxy formation models and the SMBHB population synthesis models therein.

6.1 Hierarchical Approach

We showed that by solely relying on the Hierarchical approach, it is possible to discriminate between different SMBHB population models from a noisy stochastic background. Our discrimination ability, using the stochastic background alone, depends on the instrumental noise levels. Thus far, we have used a Gaussian noise model to mimic the instrument noise of LISA, but it is needless to mention that such noise model is not the most realistic approach. A more sophisticated noise model will also account for the frequency dependence of the instrumental noise, and even the presence of other sources of gravitational waves that can affect the stochastic background.

On the other hand, in this work, we have considered one semi-analytic galaxy formation model (from Klein et al. (2016)) and the three SMBHB population realizations based on it. Hence, another caveat is our inability to span the galaxy/SMBHB evolution hyper-parameter space properly. In other words, we have not yet included enough SMBHB models, so that our Hierarchical approach faces the full challenge of discriminating between multiple SMBHB population models in light of the degeneracies.

There are various semi-analytical galaxy formation models available in the literature, each one (possibly) with multiple realizations for the population of SMBHBs. In the expected scenario of detecting a stochastic GW background with LISA (or other instruments, e.g. Decigo), we want to compare the signal against all the plausible available semi-analytic galaxy formation models (and the SMBHB populations inferred from them); this ensures of minimizing the experimenter biases in selecting the most likely model. Hence, it is essential to include all the plausible models in our analysis, and (pre) assess our ability to discriminate between these models as a function of instrument noise and systematics.

Despite the mentioned caveats, the Hierarchical approach promotes optimism for our ability to use the stochastic background as an independent probe of cosmology, large scale structure and galaxy formation. Even though we have yet to include many more galaxy formation models in our analysis, most of the different models differ in many fundamental aspects. They predict significantly different SMBHB populations, which results in a notable difference in their predictions for the stochastic background. Hence, given the availability of such models, our concerns regarding the degeneracies are slightly pessimistic. However, in the ideal scenario, we want a high-resolution span of the semi-analytic galaxy/SMBHB coevolution parameter space by numerous models, which will inevitably resurface our concerns regarding the degeneracies. Nevertheless, the satisfying performance of this approach in distinguishing between the SMBHB population synthesis models, by relying solely on the stochastic background in the LISA frequency (and not Decigo) range, is promising.

Another benefit is the inexpensive nature of this approach. Semi analytic galaxy formation models, by their simplified prescriptions, provide a fast tool compared to hydrodynamical models, to probe different Universes with different fundamental assumptions and cosmologies, which enables us to span a broad range in the parameter space with high resolution. In practice, this convenience will become exceptionally crucial, since using our approach here, it will become possible to pinpoint the highest-significance part(s) of the parameter space by an initial low-resolution assessment of the stochastic background, and follow-up semi-analytic simu-

lations can only focus on spanning the pinpointed range of the parameter space.

6.2 Recovering the Distribution

In addition to the Hierarchical approach, we also developed a MCMC sampler to recover the distribution of SMBHBs over the mass and redshift spaces. There are two reasons for this approach. First, this is useful as a standalone method to recover the distribution of SMBHBs. And second, we can use it to check its consistency with our direct-comparison approach. In what follows, we will have a more detailed discussion on both of these points.

Increasing the number of mass and redshift bins increases the computation time of our sampling method, drastically. Hence, we have limited ability in recovering the distribution of SMBHBs over the mass and redshift spaces with a high resolution. However, a more careful treatment of the underlying code, and using more horse-power will enable us to increase the dimensions of our system drastically, which as a result increases our ability in recovering a high-resolution distribution of SMBHBs from the stochastic background.

Despite the promise of directly recovering the population without relying on any specific SMBHB population synthesis model, there exist some challenges, yet to overcome. As mentioned above, on paper, it is straightforward to increase the dimensions of our MCMC sampler. But we want to stress that such scaling will have adverse effects on the accuracy of the outcome. Increasing the number of dimensions, or in other words, increasing the number of mass and redshift bins for which we want to recover the number density of SMBHBs, will increase the dimensions of the parameter space, without any data improvements (as data remains the same resolved stochastic background). This increase in the parameter space dimensions will cripple our ability to accurately constrain the number density of SMBHB in any mass and redshift bin. There is, however, an optimal number of mass and redshift bins that can balance the resolution (number of bins) with the accuracy of the recovered number density in each bin. Such optimal number of bins depends on various features of the data (stochastic background) as well as the correct SMBHB populations; for example, it depends on the resolution of the GW detector in detecting the stochastic background - roughly defined as the number of data points that the GW detector returns as the "detected" stochastic background, and also, the level of noise on the detected stochastic background.

The most promising aspect of recovering the distribution is checking the consistency of both methods (Hierarchical approach, and MCMC) in discriminating between the SMBHB population synthesis models. The accuracy of the recovered number density, especially in the intermediate mass and redshift bins, is enough for a valuable consistency check with the Hierarchical approach. However, as is the case for the Hierarchical approach, we expect this method to suffer from degeneracies by increasing the number of SMBHB population models under study.

6.3 Individually Resolved Binaries

Throughout this work, we pointed at two main observational challenges that will undermine our ability in discriminating between SMBHB population synthesis models and recovering their cosmic distribution: 1) the limited frequency range of LISA and 2) the instrumental noise and biases.

Entirely relying on the stochastic background in the LISA frequency range, cripples our ability in recovering the number density of SMBHBs in the lowest and highest mass bins as well as the lowest and highest redshift bins. We showed that a drastic improvement in the constraints on the number density of SMBHBs in the lowest mass and redshift bins is possible by including the stochastic background in Decigo frequency range. However, the technical barriers will complicate a practical implementation of such approach; we will need a careful treatment of noise profiles and systematics for each instrument to be able to combine the detections of the stochastic background from both of them.

Regarding the instrumental noise, as shown for the case of Hierarchical approach, by increasing the Gaussian noise to around 10% levels, we will lose our ability to discriminate between different models by only relying on the stochastic background emission.

However, we also provided a complementary method for overcoming these observational difficulties. We showed that it is possible to use the detections of individually resolved binaries to enhance our ability in discriminating between the different SMBHB population synthesis models from a noisy detection of the stochastic GW background. Ideally, we can implement this approach in our algorithm for recovering the distribution of SMBHBs, as well.

However, we still face some complications regarding the credibility of our approach. We divided the mass and redshift space into one hundred equal bins and assumed that, in practice, for each individually resolved binary, we know its corresponding bin. This assumption is worth some

further investigation. It is true that by dividing the mass-redshift space into 100 bins we intentionally decrease our resolution in recovering the mass and redshift of an individually resolved binary; but, this might still be a strong assumption. Especially for the case of high redshift merger events, localization of the binary in the sky will become less constrained; as a result, our ability to recover the mass and redshift of such events will drastically diminish. Hence, assuming that we will know the corresponding mass-redshift bin of the high-redshift individually resolved binaries is a strong assumption which needs modification. The most straightforward approach can be a further decrease in resolution by dividing the mass-redshift space into fewer bins. However, a more sophisticated approach would be modifying the bin sizes in response to our pre-assessment of our localization ability. In simpler terms, we can have wider bins for high-redshift and smaller bins in lower-redshift bins and again can assume that we will know the corresponding bin for each event.

Moreover, there is another caveat that we should address. Dividing the mass-redshift space into equal bins raises a technical problem: the probability of having an individually resolvable merger in each bin is not necessarily larger than a couple of percents. In some bins, the probability of having a merger event is neither negligible nor big enough ("intermediate bins" from now on). In practice, this complicates our statistics, since the probability of these intermediate bins adds up to a high enough probability in a "compound bin". From our simulations we will predict some merger events in those compound bins and assume knowing their corresponding bin (in the initially divided mass-redshift space) for deriving our priors. As a result, our simulated observations have detection peaks in bins that are not supposed to have a peak, since the correct SMBHB model will suggest that these bins were not likely to have a merger event (but instead summing them to a compound bin was). While calculating the chi-squared for discriminating between different models, we will treat these abnormal peaks in observations as a sign that the correct SMBHB population model can not be responsible/predict such peaks; this will undermine our ability to distinguish between SMBHB models based on the individually resolved binaries.

We can solve this issue by a careful treatment of these intermediate bins and attaching them to the closest high probability bin; doing this, will be straightforward for the SMBHB models studied in this work. But a drastic increase in the number of models under study requires an algorithm capable of automatically recognizing such scenarios and re-binning the mass-redshift space to avoid the mentioned complications.

Conclusion

We introduced two methods for using the stochastic GW background from the supermassive black hole binary mergers to discriminate between different SMBHB population synthesis models in Klein et al. (2016), which are based on the semi-analytic galaxy formation model introduced by Barausse (2012). First, by employing a Hierarchical Bayesian approach, we distinguished between the different models by using the stochastic background in LISA frequency range. We showed that it is possible to rely on the stochastic background detected by LISA with up to around 10% instrument noise (depending on the correct SMBHB population synthesis model) to discriminate between different SMBHB population synthesis models.

Moreover, we developed an MCMC algorithm to use the stochastic background for recovering the distribution of SMBHBs over the mass and redshift spaces. We showed that it is possible to recover the number density of SMBHB merger events in the intermediate mass and redshift bin from the stochastic background in LISA frequency range. We also showed a drastic improvement in constraining the lower mass and redshift bins by including the stochastic background in higher frequencies (from Decigo). We compared the results of the Hierarchical and MCMC methods as a way to check the consistency of our approaches against each other.

Moreover, by simulating the observations of individually resolved binaries, we showed that it is possible to derive another constraint on the SMBHB population synthesis models, from the observed distribution of individually resolved binaries. Including the constraints from the individually resolved binaries provided us with stronger overall constraints on the SMBHB population synthesis models from the combined data of the stochastic GW background and the individually resolved binaries.

Future Prospects

As mentioned in the discussion chapter, there are some complications and caveats that we will address before publishing a paper on this work. The most important issue is the observational noise model that we used to simulate the detected stochastic GW background by an upcoming survey (like LISA or Decigo). As discussed, the Gaussian noise model is the most straightforward assumption, and we want to communicate this assumption with other members of LISA collaboration. Such communication can eventually result in a more sophisticated LISA noise model, accounting for the instrumental characteristics. Also, there was a mention of uncertainty in the number of data points that LISA will return as the detected stochastic GW background; we will address this issue in our collaboration with other LISA members as well.

As mentioned in 6.3, we are suspicious of our optimistic assumption in knowing the exact low-resolution mass-redshift bin to which an observed individually resolved binary belongs; we discussed that this would not necessarily be the case, especially for high-redshift events where the sky localization is not possible. Such assumption, if optimistic, can cause an over-estimation of our capabilities in distinguishing between different SMBHB population synthesis models based on the observations of individually resolved binaries. We are planning a careful treatment of the issue, in light of which, we will update our binning mechanism by having bigger bins (less resolution) in the higher redshift bins, and smaller bins (more resolution) for the lower mass bins.

On the technical side, we are planning a collaboration with experts, to fact-check some of the chi-squared functions and statistical assumptions throughout this work.

Also, as discussed, we want to develop further the algorithm used to

derive the constraints from the detections of individually resolved binaries, to enable it to handle the predicted intermediate probability bins challenge (refer to section 6.3). We have already developed such algorithm which is capable of detecting the intermediate probability bins (predicted by SMBHB population synthesis models), and redistribute/reshape the bins if necessary. What remains is the implementation of this algorithm in the main body of the algorithm that we used to derive the constraints from the individually resolved binaries.

Furthermore, we have used the constraints derived from the individually resolved binaries to improve our Hierarchical approach; but we can (and plan to) also use them to improve the recovered population of SMBHBs.

Finally, to better span the parameter space of the semi-analytic galaxy formation models and the SMHB population synthesis models based on them, we will include more galaxy formation and SMBHB population synthesis models in our work. Currently, we have access to the semi-analytic simulations and SMBHB population realization introduced in Dayal et al. (2019). Moreover, we are planning a broader collaboration with other groups to get access to more models. Including these models in our Hierarchical framework will be the subject of a second paper.

Acknowledgments

This work would not become possible without the beautiful, and original idea of Dr Elena M. Rossi, and her trust in my capabilities in allocating the project to me. I genuinely appreciate her strong and proven support throughout the reoccurring scientific, academic, and personal complications. I am also very thankful for the level of freedom and independence that I have been offered by Dr Rossi, which allowed for the development of some very crucial skills, pivotal for the rest of my career. As I have not properly done it before, I want to acknowledge my sincere gratitude to Dr Alessandro Sonnenfeld, who I worked with during the first year of my studies; I owe most of my computational, practical, and Bayesian skills to his guidance, continues effort, and patience in training and mentoring me throughout the past two years. Many thanks to Dr Valeriya Korol, for her help and correspondence in calculating the characteristic features of the individually resolved binaries. My appreciation to Dr Matteo Rizatto for our helpful discussions on MCMC algorithms and Hierarchical Bayesian formalism. Many thanks to MSc. Martina Toscani for her time and correspondence during the initial steps of this work, especially regarding the theoretical background. My genuine appreciation for the discussions with Dr Edward N. Taylor, who, although as part of the communications for other purposes, had a significant role in my understanding of the problem. Finally, my gratitude to Prof. Paul van der Werf for agreeing to be the second reader of my thesis.

References

- Abbott B. P., et al., 2016a, *Physical Review Letters*, 116, 061102
- Abbott B. P., et al., 2016b, *Physical Review Letters*, 116, 241103
- Abbott B. P., et al., 2017, *Physical Review Letters*, 118, 221101
- Agarwal B., Khochfar S., Johnson J. L., Neistein E., Dalla Vecchia C., Livio M., 2012, *Monthly Notices of the Royal Astronomical Society*, 425, 2854 2871
- Antonini F., Barausse E., Silk J., 2015a, *The Astrophysical Journal*, 806, L8
- Antonini F., Barausse E., Silk J., 2015b, *The Astrophysical Journal*, 812, 72
- Barausse E., 2012, *Monthly Notices of the Royal Astronomical Society*, 423, 2533 2557
- Barausse E., Bellovary J., Berti E., Holley-Bockelmann K., Farris B., Sathyaprakash B., Sesana A., 2015, *Journal of Physics: Conference Series*, 610, 012001
- Bardeen J. M., 1970, *Nature*, 226, 64
- Begelman M. C., Blandford R. D., Rees M. J., 1980, *Nature*, 287, 307
- Begelman M. C., Volonteri M., Rees M. J., 2006, *Monthly Notices of the Royal Astronomical Society*, 370, 289 298
- Belczynski K., Buonanno A., Cantiello M., Fryer C. L., Holz D. E., Mandel I., Miller M. C., Walczak M., 2014a, *The Astrophysical Journal*, 789, 120
- Belczynski K., Buonanno A., Cantiello M., Fryer C. L., Holz D. E., Mandel I., Miller M. C., Walczak M., 2014b, *The Astrophysical Journal*, 789, 120
- Belczynski K., Repetto S., Holz D. E., O'Shaughnessy R., Bulik T., Berti E., Fryer C., Dominik M., 2016, *The Astrophysical Journal*, 819, 108
- Benson A. J., 2010, *Physics Reports*, 495, 33 86

- Berti E., et al., 2015, *Classical and Quantum Gravity*, 32, 243001
- Bromm V., Coppi P. S., Larson R. B., 2002, *The Astrophysical Journal*, 564, 23
- Christensen N., 2018, *Reports on Progress in Physics*, 82, 016903
- Cole S., Lacey C. G., Baugh C. M., Frenk C. S., 2002, *Monthly Notices of the Royal Astronomical Society*, 319, 168 204
- Cole S., Helly J., Frenk C. S., Parkinson H., 2008, *Monthly Notices of the Royal Astronomical Society*, 383, 546
- Colpi M., 2014, *Space Science Reviews*, 183, 189 221
- Damour T., Taylor J. H., 1992, *Physical Review D*, 45, 1840
- Dayal P., Rossi E. M., Shiralilou B., Piana O., Choudhury T. R., Volonteri M., 2019, *Monthly Notices of the Royal Astronomical Society*, 486, 2336
- Dosopoulou F., Antonini F., 2017, *The Astrophysical Journal*, 840, 31
- Dotti M., Ruszkowski M., 2010, *The Astrophysical Journal*, 713, L37 L40
- Einstein A., 1918, *Sitzungsberichte der Königlich Preußischen Akademie der Wissenschaften (Berlin)*, pp 154–167
- Fan X., et al., 2001, *The Astronomical Journal*, 122, 2833
- Ferrarese L., Merritt D., 2000, *The Astrophysical Journal*, 539, L9 L12
- Foster R. S., Backer D. C., 1990, *Astrophysical Journal*, 361, 300
- Gair J. R., Vallisneri M., Larson S. L., Baker J. G., 2013, *Living Reviews in Relativity*, 16, 7
- Granato G. L., De Zotti G., Silva L., Bressan A., Danese L., 2004, *The Astrophysical Journal*, 600, 580 594
- Haiman Z., Kocsis B., Menou K., 2009, *The Astrophysical Journal*, 700, 1952 1969
- Hulse R. A., Taylor J. H., 1975, *The Astrophysical Journal Letter*, 195, L51
- Kawamura S., et al., 2011, *Classical and Quantum Gravity*, 28, 094011
- King A. R., Pringle J. E., 2006, *Monthly Notices of the Royal Astronomical Society*, 373, L90
- Klein A., et al., 2016, *Physical Review D*, 93, 024003
- Kormendy J., Richstone D., 1995, *Annual Review of Astronomy and Astrophysics*, 33, 581
- Koushiappas S. M., Bullock J. S., Dekel A., 2004, *Monthly Notices of the Royal Astronomical Society*, 354, 292 304

- Kramer M., et al., 2006, *Science*, 314, 97
- Lacey C., Cole S., 1993, *Monthly Notices of the Royal Astronomical Society*, 262, 627
- Lodato G., Natarajan P., 2006, *Monthly Notices of the Royal Astronomical Society*, 371, 1813–1823
- Lodato G., Nayakshin S., King A. R., Pringle J. E., 2009, *Monthly Notices of the Royal Astronomical Society*, 398, 1392–1402
- Madau P., Rees M. J., 2001, *The Astrophysical Journal Letter*, 551, L27
- Maggiore M., 2008, *Gravitational Waves: Volume 1: Theory and Experiments*. Gravitational Waves, OUP Oxford, <https://books.google.nl/books?id=AqVpQgAACAAJ>
- Maio U., Ciardi B., Dolag K., Tornatore L., Khochfar S., 2010, *Monthly Notices of the Royal Astronomical Society*, 407, 1003
- Maio U., Dotti M., Petkova M., Perego A., Volonteri M., 2013, *The Astrophysical Journal*, 767, 37
- Parkinson H., Cole S., Helly J., 2007, *Monthly Notices of the Royal Astronomical Society*, 383, 557–564
- Phinney E. S., 2001, arXiv e-prints, pp astro-ph/0108028
- Plowman J. E., Jacobs D. C., Hellings R. W., Larson S. L., Tsuruta S., 2010, *Monthly Notices of the Royal Astronomical Society*, 401, 2706–2714
- Schaye J., et al., 2015, *Monthly Notices of the Royal Astronomical Society*, 446, 521
- Sesana A., Gair J., Berti E., Volonteri M., 2011, *Physical Review D*, 83
- Sesana A., Barausse E., Dotti M., Rossi E. M., 2014, *The Astrophysical Journal*, 794, 104
- Shapiro S. L., 2005, *The Astrophysical Journal*, 620, 59
- Silk J., Mamon G. A., 2012, *Research in Astronomy and Astrophysics*, 12, 917–946
- Siwek M. S., Kelley L. Z., Hernquist L., 2020, The effect of differential accretion on the Gravitational Wave Background and the present day MBH Binary population (arXiv:2005.09010)
- Springel V., et al., 2005, *Nature*, 435, 629
- Taffoni G., Mayer L., Colpi M., Governato F., 2003, *Monthly Notices of the Royal Astronomical Society*, 341, 434–448

- Tanaka T., Haiman Z., 2009, *The Astrophysical Journal*, 696, 1798
- Thorne K. S., 1974, *The Astrophysical Journal*, 191, 507
- Thrane E., Talbot C., 2019, *Publications of the Astronomical Society of Australia*, 36, e010
- Toomre A., 1977, in Tinsley B. M., Larson Richard B. Gehret D. C., eds, *Evolution of Galaxies and Stellar Populations*. p. 401
- Vasiliev E., Antonini F., Merritt D., 2014, *The Astrophysical Journal*, 785, 163
- Vasiliev E., Antonini F., Merritt D., 2015, *The Astrophysical Journal*, 810, 49
- Volonteri M., 2010, *The Astronomy and Astrophysics Review*, 18, 279 315
- Volonteri M., Rees M. J., 2006, *The Astrophysical Journal*, 650, 669
- Volonteri M., Haardt F., Madau P., 2003, *The Astrophysical Journal*, 582, 559
- Weinberg S., 1972, *Gravitation and Cosmology: Principles and Applications of the General Theory of Relativity*
- Yunes N., Siemens X., 2013, *Living Reviews in Relativity*, 16, 9